Organic Photovoltaic Spectral Coverage Improvement

ORGANIC PHOTOVOLTAIC SPECTRAL COVERAGE IMPROVEMENT

BY

NATHAN M. BAMSEY, B.Eng.Mgt.

A THESIS
SUBMITTED TO THE DEPARTMENT OF ENGINEERING PHSYSICS
AND THE SCHOOL OF GRADUATE STUDIES
OF MCMASTER UNIVERSITY
IN PARTIAL FULFILMENT OF THE REQUIREMENTS
FOR THE DEGREE OF
MASTER OF APPLIED SCIENCE

Master of Applied Science (2010)
(Engineering Physics)

McMaster University
Hamilton, Ontario, Canada

TITLE:	Organic Photovoltaic Spectral Coverage Improvement
AUTHOR:	Nathan M. Bamsey B.Eng.Mgt., (Materials Engineering & Management) McMaster University, Hamilton, Ontario, Canada
SUPERVISOR:	Dr. John S. Preston & Dr. Rafik Loutfy
NUMBER OF PAGES:	xiv, 93

to my parents, whose guidance and support has built the foundation upon which I can stand.

Abstract

Methods for improving spectral absorption and efficiency of phthalocyanine based organic photovoltaic devices were investigated. New structures including simple tandem architectures and a novel heteromorphic phthalocyanine (MPc) device were investigated and characterized. The addition of an interlayer of MPc was shown to improve efficiencies of solution based bulk heterojunction devices due to improved open circuit voltage (V_{oc}) and spectral absorption. Solvent treatment has been shown to be an effective method for extending absorption characteristics of trivalent and tetravalent phthalocyanine based solar cells into the near infrared due to polymorphic conversion. Heteromorphic devices incorporating two distinct polymorphs of the same MPc resulted in optimal device characteristics while retaining relative simplicity in fabrication techniques. In this configuration, short circuit current density (J_{sc}) was enhanced considerably while V_{oc} retained an intermediary voltage between both the control and fully treated devices. Improved spectral response at longer wavelengths had a direct impact on J_{sc} in solvent treated devices and was a key factor in improved device efficiency. Characterization of new device structures was performed using current-voltage (I-V) measurements, external quantum efficiency (EQE) and a Scanning Electron Microscope (SEM).

Acknowledgements

Without the incredibly generous assistance of a great many people this journey would not have been possible.

I would like to thank Xerox Research Centre of Canada for their partnership and generous research support throughout my studies. I would also like to show my gratitude to my colleagues at XRCC for their consistently helpful input along the way.

I owe a considerable amount to a variety of people for their openness and sharing of ideas. Thank you to Ah-Mee Hor for your welcoming attitude and offering your vast experiential knowledge. Vlad Skorokhod I am grateful for your openness to questions, Dr. Rafik Loutfy thank you for sharing some of your technical experience. Dr. John Preston I am grateful for your persistent attention to detail and for always seeing the lighter side of any situation.

I would certainly like to thank all of my colleagues at McMaster University.

Jennifer Khan and Dr. Gino Ferri you have inspired growth and knowledge in me in so many ways it would be impossible for me to fit them here. Your constant selfless caring for other people is something all should aspire for.

I owe a great deal of thanks to Richard Klenkler and Avery Yuen whose mentorship and guidance will never be forgotten and were a vital part of this work and my own personal growth.

Finally, I will forever be indebted to my parents. Thank you for your unwavering encouragement and love.

Notation and Abbreviations

BCP	Bathocuproine
ClAlPc	Chloroaluminum Phthalocyanine
ClGaPc	Chlorogallium Phthalocyanine
ClInPc	Chloroindium Phthalocyanine
CuPc	Copper Phthalocyanine
DI	Deionized
EBL	Electron Blocking Layer
EQE	External Quantum Efficiency
FF	Fill Factor
H_2Pc	Metal-free Phthalocyanine
HOMO	Highest Occupied Molecular Orbital
I-V	Current-Voltage
ITO	Indium-Tin-Oxide
J-V	Current Density-Voltage
I_{sc}	Short Circuit Current
J_{sc}	Short Circuit Current Density
LUMO	Lowest Unoccupied Molecular Orbital

MEH-PPV	Poly(2-methoxy-5-(2'-ethylhexyloxy)-1,4-phenylvinylene)
MgPc	Magnesium Phthalocyanine
MPc	Metal Phthalocyanine
OD	Optical Density
OFET	Organic Field Effect Transistor
OPV	Organic Photovoltaics
P3HT	Poly(3-hexylthiophene)
PCBM	[6,6]-Phenyl-C_{61}-Butyric Acid Methyl Ester
PCE	Power Conversion Efficiency
PEDOT:PSS	Poly(3,4-ethylenedioxythiophene):poly(styrene-sulfonic acid)
PIN	*p*-i-*n* (*p*-type, intrinsic, *n*-type)
PQT-12	Poly(3,3'''-didodecyl quaterthiophene)
PV	Photovoltaic
SEM	Scanning Electron Microscope
THF	Tetrahydrofuran
TiOPc	Titanyl Phthalocyanine
TOF	Time-of-Flight
TOF-SIMS	Time-of-Flight Secondary Ion Mass Specroscopy
VOPc	Vanadyl Phthalocyanine
V_{oc}	Open Circuit Voltage
XRCC	Xerox Research Centre of Canada
XRD	X-ray Diffraction
ZnPc	Zinc Phthalocyanine

Contents

List of Figures

Chapter 1

Introduction

1.1 Photovoltaic Devices

The potential for solar cell technology in today's industry is quite pronounced. Photovoltaics (PV) can cleanly convert light into usable energy without any moving parts or noise. Modules may be placed almost anywhere and can be installed relatively simply in any scale. Efficiencies of photovoltaic devices have been increasing steadily since their discovery in the 1950s and today are increasingly used as a method of economic energy production. Research in this field has and will continue to enhance this technology.

1.1.1 The I-V Curve

The equivalent circuit of an ideal solar cell can be described as a current source connected in parallel with a rectifying diode, as in Figure 1.1 [1]. Correspondingly, the Current-Voltage (I-V) curve is described by the Shockley solar cell equation:

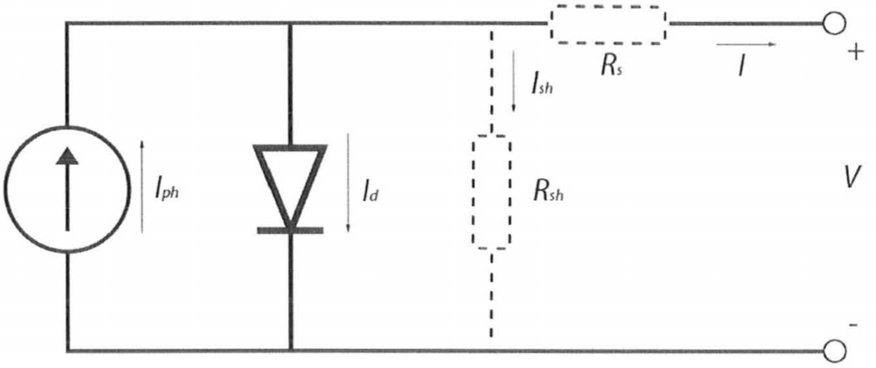

Figure 1.1: Equivalent circuit of an ideal solar cell (solid lines). Non-ideal components are also shown (dotted lines).

$$I = I_{ph} - I_0(\exp^{\frac{qV}{k_\beta T}} - 1) \tag{1.1}$$

where q is the electron charge ($q > 0$), V is the voltage across the cell, k_β is the Boltzman constant and T is the absolute temperature. I_0 is the reverse saturation current and I_{ph} is directly related to the incident photon flux on the solar cell. If the electrodes are short-circuited via a metal contact, then the current flowing through the system is a function of optically generated charge, and is known as the short circuit current (I_{sc}). In the ideal case, the short circuit current would be equal to the photogenerated current:

$$I_{sc(ideal)} = I_{ph} \tag{1.2}$$

The open circuit voltage (V_{oc}) in a solar cell is the potential difference generated between the opposite electrodes when there is no external load applied to the cell and the circuit is 'open'. Optically generated charges build up, creating an electric field until an equilibrium point is reached where the rate of charge generation is equal to the rate of recombination within the cell.

$$V_{oc(ideal)} = \frac{k_{\beta}T}{q}\ln(1+\frac{I_{ph}}{I_0}) \tag{1.3}$$

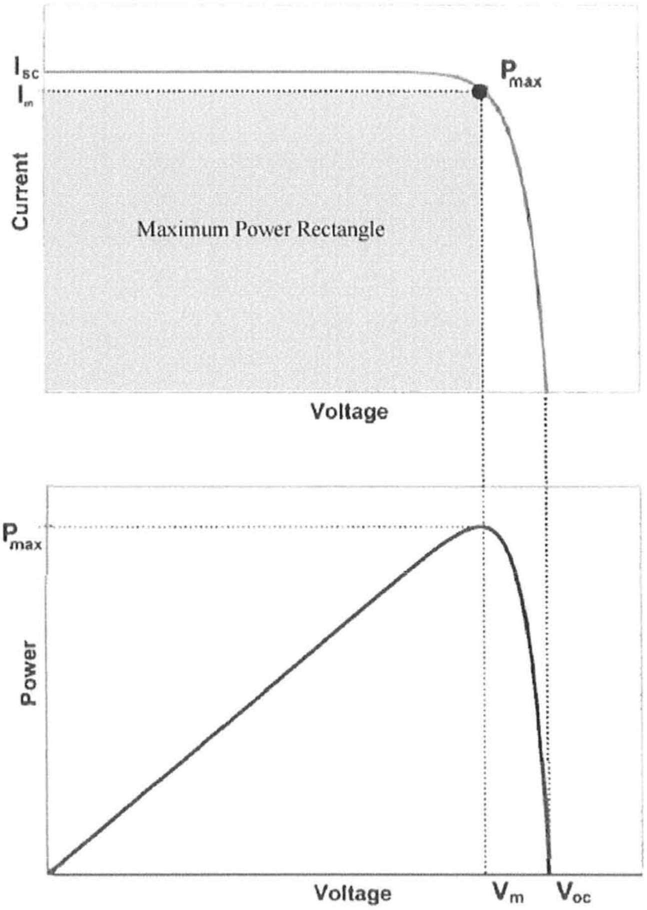

Figure 1.2: (a) I-V curve of a typical solar cell and b) power generated by the cell with the maximum power point identified.

The maximum power point, seen in Figure 1.2 occurs where the product of current and voltage is highest [1]. This is the point where maximum energy can be extracted from the cell under illumination. Another associated parameter used to define the shape of the I-V curve is the fill factor (FF). This term given in percentage describes the squareness of the I-V curve. The higher the FF the more square the I-V shape and the higher the maximum power point. The FF is given by the equation:

$$FF = \frac{I_m V_m}{I_{sc} V_{oc}} = \frac{P_{max}}{I_{sc} V_{oc}} \tag{1.4}$$

In practice, cell characteristics and I-V curve shape differ from ideality. The equivalent circuit must be modified to include several new components as seen by dotted lines in Figure 1.1. Both the series resistance (R_s) and shunt resistance (R_{sh}) degrade the fill factor of the cell, and the direct impact on I-V characteristics can be seen in Figure 1.3 [1]. The shunt resistance originates from leakage around the cell through grain boundaries or dislocations and can be very complex to model or control [2]. Under most practical operating conditions however shunt resistance has minimal impact. The series resistance on the other hand can have a drastic impact on cell characteristics. R_s directly depends on the contact between the metal electrodes and the active layer, and also on the morphology and film quality of the active layer itself. High series resistance can dramatically reduce the fill factor of the cell, leading to significantly poorer power conversion efficiency (PCE). As can be seen, optimal series resistances should be as low as possible, while the shunt resistance should approach infinity. With poor R_s and R_{sh} the shape of solar cell I-V curve approaches that of a resistor and becomes a straight line through the origin.

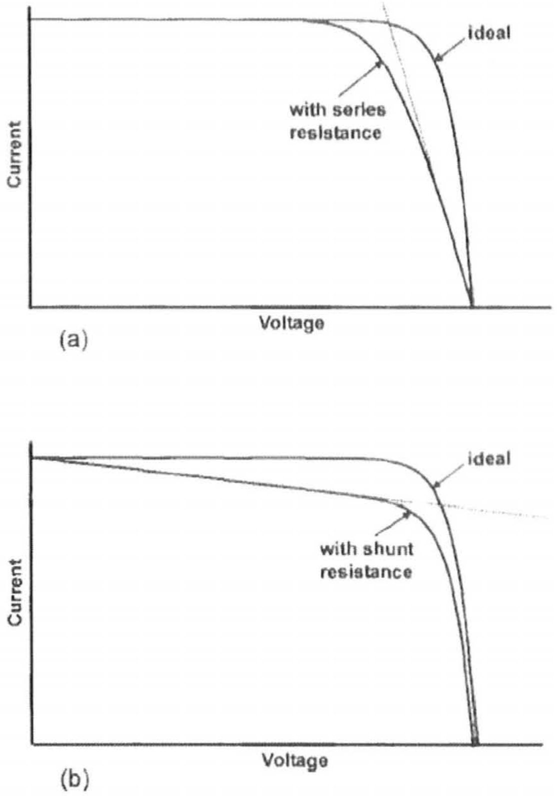

Figure 1.3: The effect of parasitic resistances on I-V characteristics.

The characteristic equation is now modified to include these components:

$$I = I_{ph} - I_d - I_{sh} = I_{ph} - I_0((\exp^{\frac{q(V+IR_s)}{k_\beta T}} - 1)) - \frac{V + IR_s}{R_{sh}} \tag{1.5}$$

I-V characterization can provide useful insight into the charge generation and transport capabilities of a fabricated cell. Understanding changes in the shape of the I-V curve is a necessary tool for revising and optimizing cell design. I-V measurements also allow accurate comparisons between the properties of individual cells.

1.1.2 EQE and Spectral Response

The External Quantum Efficiency (EQE) of a solar cell is the percentage of electrons in the external circuit produced by an incident photon flux at a given wavelength. For a particular photon energy the EQE is found by measuring the short circuit current generated at that specific photon energy and is given as:

$$EQE(\lambda) = \frac{I_{sc}(\lambda)}{qAI(\lambda)} \tag{1.6}$$

where q is the electron charge, A is the illuminated cell area in m^2, and $I(\lambda)$ is the photon flux at a particular wavelength in photons/m^{2}s. In most cases the EQE is measured over a range of wavelengths and the spectral response is plotted to understand the light absorption and charge generation across a broad spectrum. When taken over a wide enough range, the total current generated will approach the J_{sc} measured under full illumination. This can be expressed as:

$$I_{sc} = q \int_{\lambda(wide)} EQE(\lambda)\Phi(\lambda)\, d\lambda \tag{1.7}$$

where $\Phi(\lambda)$ is the photon flux in photons/s·eV.

1.2 Organic Photovoltaic Concepts

Organic Photovoltaics (OPV) is a relatively new field of research involving the generation of energy using thin films of organic molecules. There are many aspects of this technology that make it an attractive field of study. Unlike their inorganic counterparts, organic thin films are semitransparent and can be deposited onto flexible substrates. The possibility for lightweight and economical production is very attractive, as these devices have the potential to be produced in large scale using established printing techniques. Efficiencies, though still generally below the economical level for commercial products, have been steadily increasing due to continued research and new findings [3–5].

1.2.1 Semi-Crystalline Materials

Crystalline inorganic semiconductors form a three dimensional lattice structure allowing bonding and antibonding orbitals to form a continuous conduction band and valence band throughout the entire crystal [6]. The electronic properties of organic semiconductors however are fundamentally different and due to weaker orbital interaction the Highest Occupied Molecular Orbitals (HOMOs) and Lowest Unoccupied Molecular Orbitals (LUMOs) do not interact strongly to form continuous bands. Consequently excited states in organic materials are localized and proceed via hopping rather than diffusion within a band [6]. Mobilities of charge carriers in organic materials are generally lower than inorganic semiconductors and the mechanism of charge separation in organics requires more attention due to lower dielectric constants [6]. The formation of excited states in organic semiconductors almost always results in a bound electron-hole pair, known as an exciton [1]. This so-called π to π^* transition describes the promotion of a pi bond electron to that of an antibonding orbital and the energy difference matches the HOMO-LUMO gap. Excitons are generally considered to be localized, with an average diffusion distance on the nanometer scale [6]. Inorganic semiconductors however do not create these localized states since photoexcitation leads directly to charge separation because thermal energy ($\mathrm{k}T$) in conjunction with the natural bias of the device is strong enough to dissociate excitons into free charges [7]. A variety of device structures described below have been used overcome the challenge of localized excitons in OPV materials.

1.2.2 Single Layer Devices

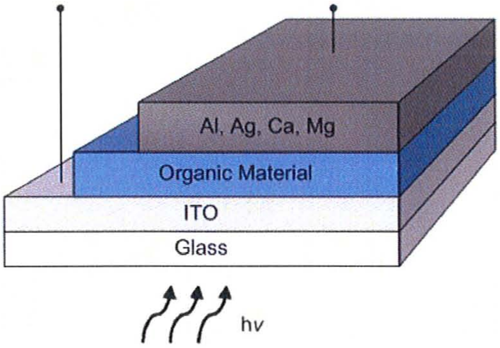

Figure 1.4: Single layer organic PV device structure.

The first organic PV devices were based on a single layer sandwiched between two metal electrodes of differing work functions as in Figure 1.4 [7]. An energy level diagram is shown in Figure 1.5 indicates the formation of a photoexcited state upon light absorption [6]. An electron is promoted to the LUMO, and a hole is left behind in the HOMO. Opposing charges are then collected at the corresponding electrodes due to the asymmetry of the metal work functions (Φ). The effective band gap (E_g) is determined by the particular semiconductor chosen. These PV devices have very limited efficiencies (well below 0.1%) due to a number of reasons. The preferential creation of excitons in organic materials is due to their comparatively low dielectric constants (ca. 2-4) and the fact that weak intermolecular forces keep excited states

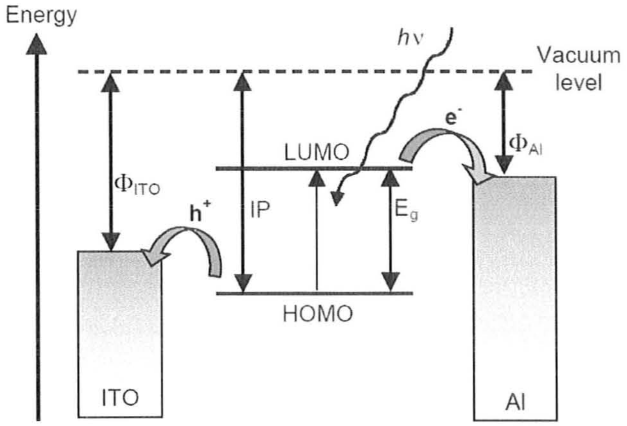

Figure 1.5: Energy level diagram for a single layer organic PV device. Light is absorbed, promoting an electron (e^-) to the LUMO leaving a hole (h^+) behind in the HOMO. Electrons are subsequently collected at the Al interface while holes are collected at the ITO electrode.

localized [7]. The asymmetrical work function of the metal electrodes is not sufficient to separate excitons in single layer devices and the low diffusion lengths of excitons in organic materials reduces the number reaching the electrodes where they can dissociate [7]. The typical diffusion lengths of about 10 nm in organic materials is generally much shorter than the device thickness and so a large number of photogenerated excitons recombine within the active layer before reaching an interface. Generated current in single layer OPVs is therefore severely limited by the availability of mechanisms for charge separation [7]. New structures and concepts in OPV research have since overcome this hurdle and are descried in the following sections.

1.2.3 Heterojunction Devices

Tang first proposed a novel device architecture in 1986 when he brought two different organic semiconducting materials into contact, creating an active bilayer interface [3]. This concept utilized two organic materials with differing electron affinities and ionization potentials, resulting in a strong field at the interface where exciton dissociation was favoured. This new structure overcame the serious limitations inherent in single layer devices. The interface of the two-layer system now became primarily responsible for the photogeneration of charge, instead of the much less efficient electrode-organic interface. Upon dissociation of excitons, holes are preferentially collected by the high work function ITO anode and electrodes are collected by the low work function metal cathode. Efficiencies can reach several percent using this donor/acceptor heterojunction structure shown in Figure 1.6. Excitons created within the diffusion distance from the interface can be separated much more efficiently than at an organic/metal interface. This interaction can be represented by Figure 1.7 showing photon absorption in the donor followed by exciton dissociation and charge

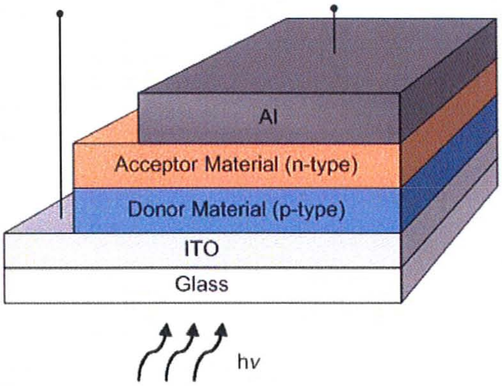

Figure 1.6: Bilayer organic PV device structure.

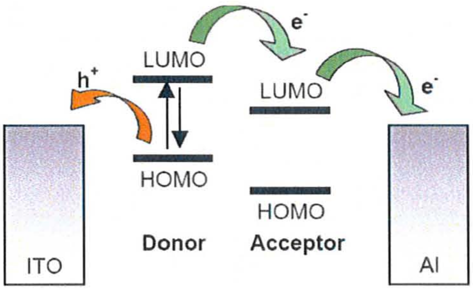

Figure 1.7: Bilayer organic PV device energy level diagram.

transfer at the interface. Electrons are donated to the acceptor material and charge collection occurs at each respective electrode [6].

1.2.4 The Bulk Heterojunction

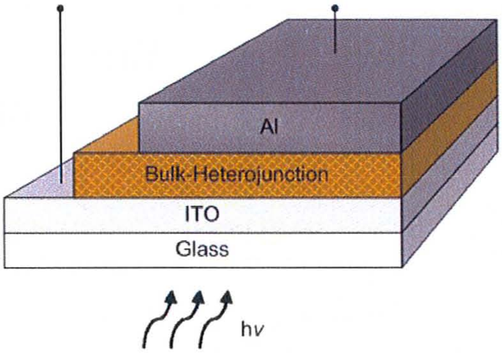

Figure 1.8: Bulk-heterojunction device structure.

Since typical exciton diffusion lengths in organic materials are in the range of 10 nm, light harvesting in bilayer cells is limited to the region close to the interface. On the other hand, for more or less complete absorption of light, organic film thicknesses should be around 100 nm [6]. This challenge can be overcome by blending the donor and acceptor either in solution or by co-evaporating the materials together during fabrication. This concept shown in Figure 1.8 creates a bulk heterojunction with extremely high interfacial area for improved charge separation. The optimal situation is a bicontinuous network of donor and acceptor material, allowing for optimal charge separation and collection. If the layer is designed such that the average distance to any interface in the film is less than the diffusion length, exciton decay processes are reduced considerably. This is because wherever an exciton is generated, it will be able to reach an interface and separate into free charges before it recombines [7]. The effective result is that charge generation can now occur throughout the active layer and is not limited to the region near the bilayer interface. Due to miscibility issues in solution, spin coating of films is typically performed at elevated temperatures using low boiling point solvents so that equilibrium is never reached. The highest single junction cell efficiencies are obtained using the bulk heterojunction principle [5,8,9].

1.3 Materials & Devices

1.3.1 Solid-State Organics: Conjugated Polymers

Traditionally, plastics have been thought of as insulators and were not generally considered electrically active materials. Since the discovery of useful electrical properties in doped conjugated polymers in the 1970s, research has developed an array of polymeric materials that can be tuned for use in a variety of optoelectronic applications [6,10]. Use of solution processable polymers in PV is attractive for a number of reasons, including inexpensive processing and high throughput using printing technologies [10]. These materials are also semitransparent and devices can be lightweight due to the low density materials used and the need for only thin films. Semiconducting polymers can combine the optoelectronic properties of traditional semiconductors with the attractive physical properties and processing capabilities of plastics [7].

Conjugated polymers all share a backbone of sp^2-hybridized carbon atoms where the electrons in the p_z orbital of each atom along the chain form π bonds with neighbouring p_z electrons [11]. Dimerization (due to Peierls distortion) creates an alternating single and double bond structure along the chain, allowing for delocalized π electrons within the molecule [12]. Photoexcitation promotes electrons to the antibonding π band (π^*) and allows for charge donation to an acceptor molecule [12,13].

Organic semiconductors differ somewhat from their inorganic counterparts. The exciton binding energy in conjugated polymers is considerably higher (~ 0.4 eV), than in traditional semiconductors and photoexcited electrons and holes are bound by their Coulombic attraction [11]. Exciton effects become dominant at room temperature and the result is Frenkel-like excitons [7]. Exciton diffusion distances (L_D) between 5 nm and 20 nm have been found for these bound pairs [7]. Since coupling between neighbouring molecules in organic materials is low, excitations are localized and there is limited band to band transition [7]. In addition, organic materials have dielectric constants around three whereas inorganic semiconductors sit at around ten [7]. Fortunately, the high optical absorption coefficients of these materials requires only thin films. Still, without a charge separation site, the majority of excitons will recombine. This explains the limited efficiencies in single layer polymeric solar cells as there are no efficient sites for charge dissociation. The fact that there is very limited charge separation without the presence of an effective electron acceptor prevents efficiencies of single layer cells from reaching 0.1%. Since most conjugated polymers are p-type, the use of an acceptor (n-type) molecule, often [6,6]-phenyl-C_{61}-butyric acid methyl ester (PCBM) is used to ensure efficient charge separation and collection. See Section 1.3.2 for a detailed description of this material.

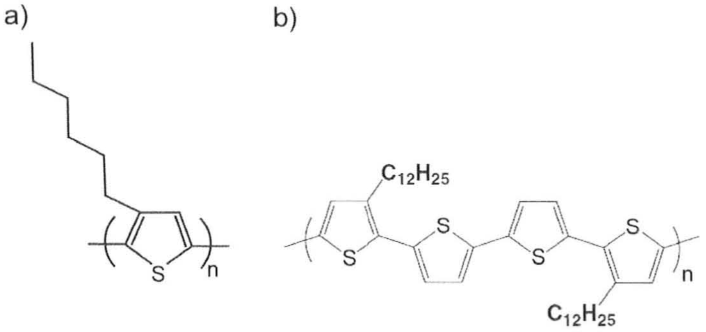

Figure 1.9: Chemical structure of a) P3HT and b) PQT-12.

One of the most commonly used conjugated polymers is poly(3-hexylthiophene) (P3HT) shown in Figure 1.9 a). P3HT is soluble in a number of organic solvents, and bulk heterojunction OPVs integrating this material as well as an acceptor have reached efficiencies as high as 5.2% [5]. Annealing is a necessary processing step during cell fabrication and is used to improve crystallinity in bulk heterojunction cells incorporating PCBM [14]. Poly(3,3'''-didodecyl quaterthiophene) (PQT-12) shown in Figure 1.9 b) is another conjugated polymer that has been less commonly used in

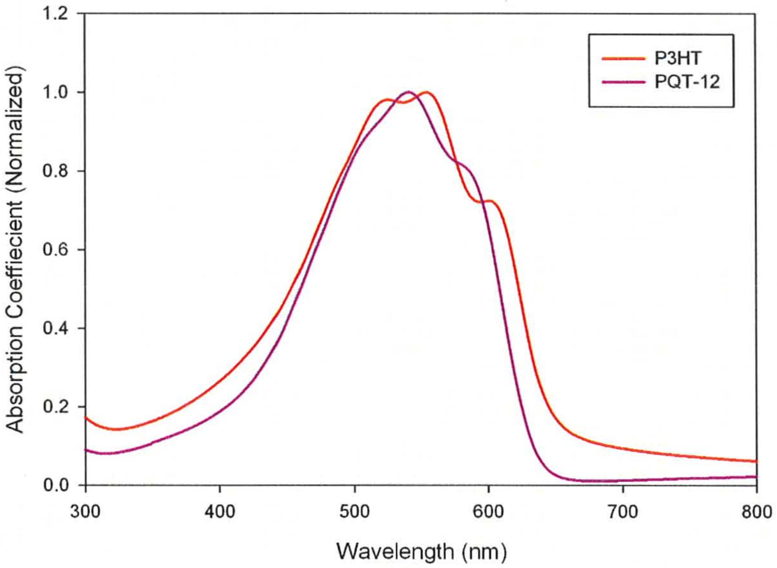

Figure 1.10: Spectral absorption of P3HT and PQT-12.

OPVs [15,16]. PQT-12 has been successfully used in Organic Field Effect Transistors (OFETs) and has demonstrated considerable stability in oxygen [17,18]. PQT-12 also has similar hole mobility and absorption characteristics to P3HT [18]. The absorption curves of both P3HT and PQT-12 are shown in Figure 1.10.

Investigating the solar spectrum shown in Figure 1.11 one can see that the majority of solar irradiance is concentrated below 2000 nm [19]. Solar irradiance and total photon flux are both adequate representations of the solar spectrum however since in most models PV devices essentially convert a single photon into a single electron, total photon flux may best represent the energy available for conversion into current under ideal conditions [19]. This approach results in a distinct red-shifting of the

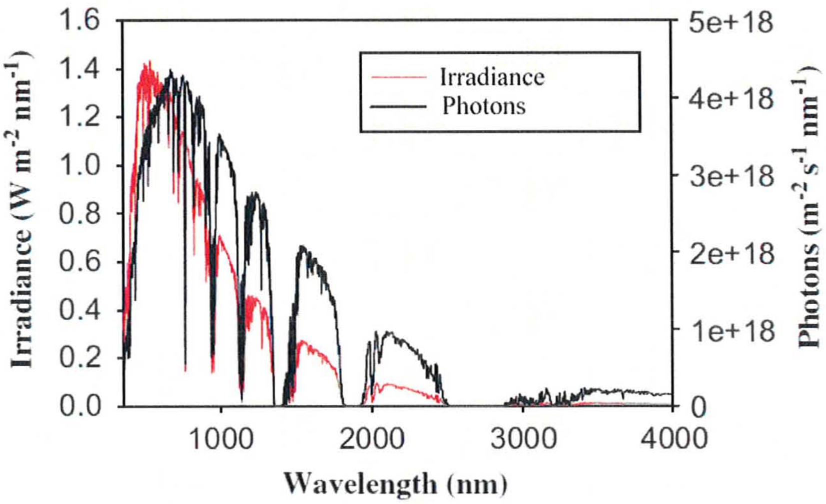

Figure 1.11: Solar irradiance (red) and number of photons (black) versus wavelength.

solar spectrum maximum and from this perspective it is more important to harvest longer-wavelength photons in PV devices. It should be noted that although the lower energy photons can limit the voltage difference in the device, there is still potential for greater total current generated. Due to this interplay in excitonic solar cells, the optimal band gap is still not clear. In any case it is clear that finding suitable low band gap materials which can extend absorption beyond 650 nm is important to improve spectral overlap and the overall efficiencies of OPVs.

1.3.2 [6,6]-phenyl-C_{61}-butyric acid methyl ester (PCBM)

Optimization of solution-processed OPVs requires the use of an acceptor (n-type) material. Often, a soluble substituted C_{60} derivative (PCBM) can be integrated into solution with the donor material creating a bulk heterojunction [20]. Unsubstituted

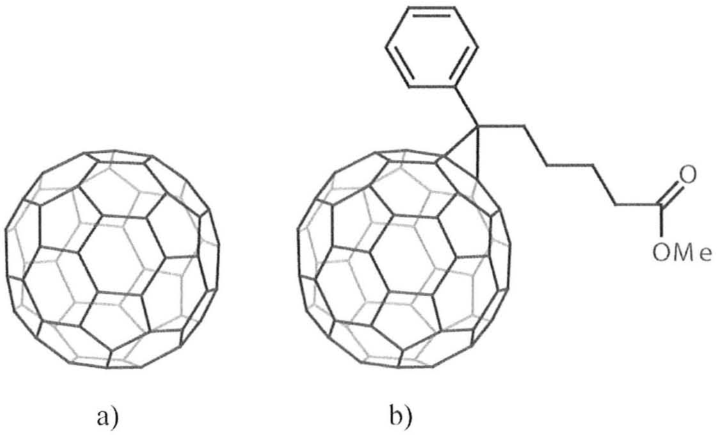

Figure 1.12: Molecular structure of a) C_{60} and b) PCBM.

C_{60} has limited solubility and must be vacuum deposited in order to be integrated into OPVs. The two varieties of fullerenes often used (shown in Figure 1.12) are electrically similar once integrated into PV cells. Fullerenes are considered optimal acceptor materials for a variety of reasons: (1) they have a high electron affinity due to the low lying LUMO level (2) each C_{60} has the ability to accept multiple electrons and (3) the electron transfer to the C_{60}/PCBM phase is ultra-fast (<200 fs) versus other competing relaxation processes in conjugated polymers, leading to a charge transfer quantum efficiency near unity [10,20]. In addition, the charge separated state in bulk heterojunctions involving these materials is metastable, allowing efficient collection of the photoexcited charges at the electrodes [12]. Fullerenes are typically treated only as acceptor molecules as they have limited energy absorption matching with the solar spectrum, seen by the absorption spectra of PCBM in Figure 1.13. Within the peak absorption range of C_{60} and PCBM, solar irradiance is low and so these materials contribute only minimally to charge generation. When creating bulk heterojunction

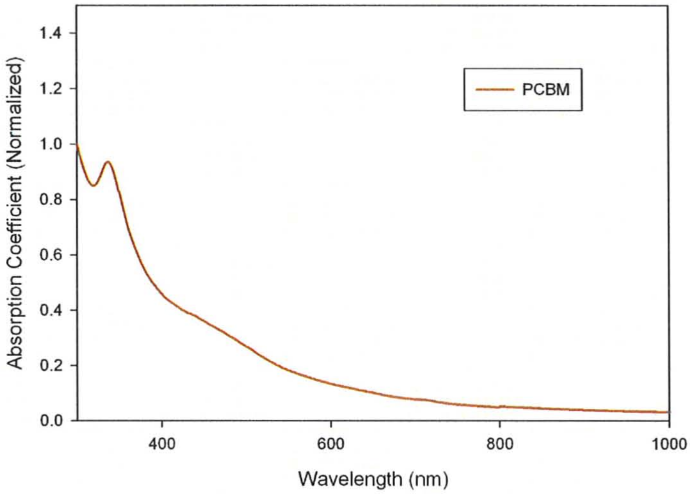

Figure 1.13: Absorption spectrum of PCBM.

devices incorporating P3HT:PCBM, a ratio near 1:1 appears to be optimal [5, 20].

1.3.3 Solid State Organics: Small-Molecule Materials

1.3.3.1 Origin and Structure of Phthalocyanines

Metallophthalocyanines (MPcs) are a class of organic small molecules, consisting of a planar ring structure of four isoindole units connected via aza nitrogen [21, 22]. The central position is occupied by two hydrogen atoms in metal-free phthalocyanine and can also be occupied by a variety of metals, metal halides or metal hydroxides [21]. The MPc structure was verified, and the X-ray single-crystal structures of several phthalocyanines were reported by Robertson and co-workers [21, 23–26]. The structure is shown in Figure 1.14, with M indicating the central metal atom, or two hydrogen atoms in case of the metal-free [21]. The simplest structures are monovalent (H_2Pc),

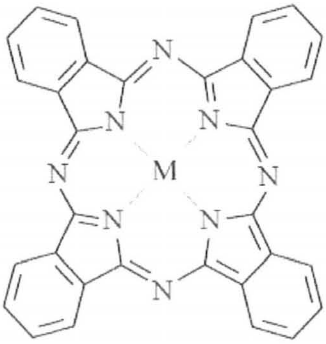

Figure 1.14: Metal Phthalocyanine (MPc) structure. *M* indicates the central atom(s).

or divalent (CuPc, MgPc, ZnPc) [21]. Trivalent metals form metal halides or hydroxides; for example ClAlPc, ClInPc and ClGaPc [21]. Tetravalent metals can also exist in the ring structure in the form of metal oxides, dihalides or dihydroxides as is the case for TiOPc, VOPc [21]. The size of the central atom directly affects the length and angle of the bonds in the surrounding ring structure. The corresponding cavity size depends on the ionic size of the metal atom, and if it is large enough, may situate slightly out of plane of the molecule [27]. This doming effect is present in tin and lead phthalocyanines.

Phthalocyanine crystals exist in a variety of polymorphs. The planar and nearly square molecular shape arrange in long columnar stacks [28]. Variations occur in the angle between the main axis and molecular axis, as well as how neighboring stacks are arranged relative to one another [29]. The variable molecular stacking arrangements lead to slightly different optical and electrical properties in the bulk material. An example of two different polymorphs of copper phthalocyanine (CuPc) is shown in

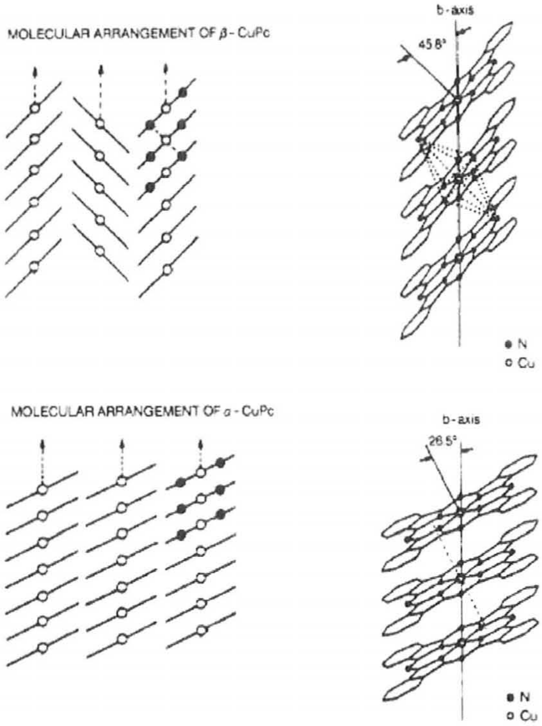

Figure 1.15: Molecular arrangements of two polymorphs of CuPc: α-CuPc and β-CuPc.

Figure 1.15 [21]. Thermodynamically, β-CuPc is the most stable polymorph however vacuum deposition at room temperature yields metastable α-phase phthalocyanine [21, 22]. Upon thermal annealing, transformation into the β-phase can be induced [22, 28]. Annealing yields phase changes in other phthalocyanines in a similar manner [30].

Within crystals of phthalocyanines, molecules are oriented such that prism surfaces are parallel to the longitudinal stacking axis [29]. The outer edges of the crystals therefore typically consist of hydrogen atoms, with the basal planes contained within [29]. As a whole, the crystal surface is largely non-polar, lending to minimal interaction with surrounding medium. This impacts the dispersibility of the pigment, particularly stabilization and surface wetting [29]. Typically these compounds display very limited hydrophilicity, and it is therefore of little surprise that they flocculate and have limited solubility in most organic solvents [29]. Stabilization against flocculation can be accomplished by introducing polar groups to the structure of the molecule [29]. MPcs are thermally stable and so can be sublimed without decomposition, allowing the preparation of thin films via vacuum evaporation [22]. CuPc shows good heat stability and since it does not melt, can be sublimed at approximately 550°C under ambient pressure [29].

Commercially, MPcs are used worldwide as an organic pigment. CuPc constitutes the vast majority of the market [29]. Dyes are produced by chemically modifying the outer hydrogen and adding solubilizing groups to the outer rings [29]. These dyes are used in particular areas of the textile and paper industry [29].

1.3.3.2 Optical Characteristics

Spectral data of many MPcs have been studied in solution and in the vapour phase [21]. Two key absorption bands; the Q-band (600-700 nm) and the Soret band ($\sim$300-400 nm) in the near-UV are important for phthalocyanines [21]. The strong Q-band absorption in the red region of the visible spectrum accounts for the blue colour of this class of materials [31]. Electrically, the central metal has a small effect on the activation energies of conduction [32]. Journals have published investigations indicating effects of central metal atom substitutions on optical properties [31]. Solid state absorption properties appear to be affected by the central metal, crystal structure and particle size, giving MPcs various optical absorption characteristics and a range of colours from dark blue to green [21]. Molecular orbital calculations show that the visible Q-band absorption results from the $\pi \rightarrow \pi^*$ transition [21]. This arises from the delocalization of the phthalocyanine ring system when the outer benzene ring transfers charge to the inner macrocyclic ring [21].

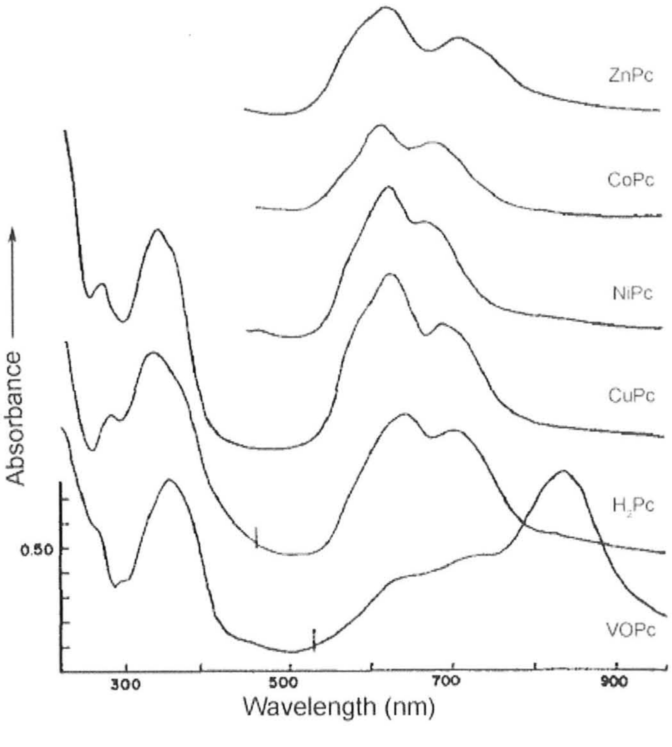

Figure 1.16: Thin film α-MPc absorption spectra.

In solid state, the various polymorphs of each MPc display slightly different absorption curves [21]. Absorption spectra of sublimed MPc films have been investigated and compared as seen in Figure 1.16 [28,30,33]. Thin-film α-phase Zn, Co, Ni, Cu, VO and metal-free phthalocyanine absorption spectra have been investigated and compared [30]. The films were deposited onto substrates at 150 °C and pressures below 3×10^{-5} Torr.

1.3.3.3 PV Characteristics

The conjugated structure of phthalocyanine molecules lead to useful electronic properties. MPcs have shown promise as electron donors (p-type) in photovoltaic devices [3,34–38]. Using small organic molecules such as MPcs in photovoltaics has several potential advantages. These molecules have considerable structural stability, and advantageous colour fastness, and with proper integration phthalocyanines could improve device lifetimes [29]. The other advantage is the variety of optical absorption characteristics that phthalocyanines possess. The strong absorption of most MPcs in the near IR can also improve overall spectral coverage of photovoltaic devices [37]. Absorption curves of P3HT and C_{60} drop off considerably around 650 nm so capturing wavelengths above those absorbed by P3HT and C_{60} by using MPcs could better match device absorption to the solar spectrum [39].

Device architectures typically consist of thin evaporated films of pure or mixed layers containing MPcs and other semiconducting materials. Device structures can also utilize a charge separating heterojunction at the interface of two films of materials (p,n) as seen in Figure 1.17 [40]. Bathocuproine (BCP) and Poly(3,4-ethylenedioxythiophene) poly(styrenesulfonate) (PEDOT:PSS) are described in more detail in Section 1.5.1. Bulk heterojunctions are formed by co-evaporating MPcs concurrently

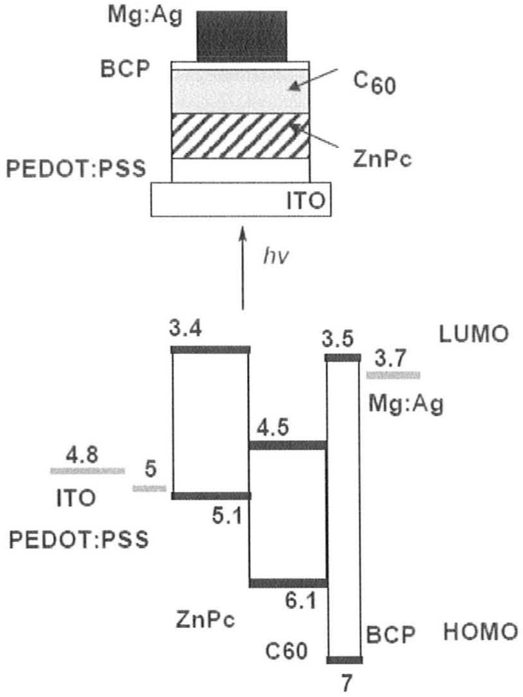

Figure 1.17: Structure and energy levels of an MPc bilayer PV device.

with an n-type acceptor molecule [40]. C_{60} is one of the most commonly used n-type materials with suitable electronic properties [34]. Bulk heterojunctions offer the advantage of an extremely large interfacial surface area, allowing improved charge separation and collection, resulting in more efficient device performance [6].

MPcs have also been integrated into solution-based photovoltaic devices [37]. In this case the phthalocyanine molecule is typically modified to allow for much greater solubility in organic solvents, and is then spin coated [37, 39]. Figure 1.18 shows the absorption of a spun polymer, dye, and metal-free phthalocyanine film compared to

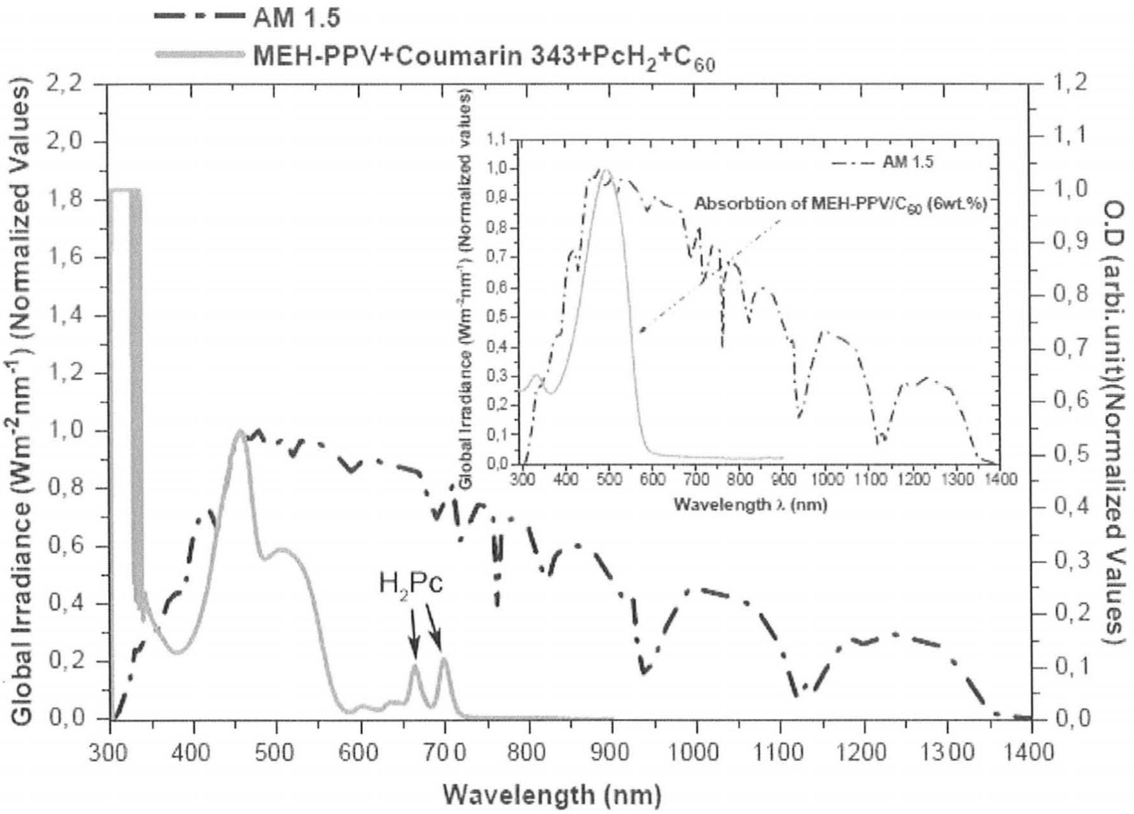

Figure 1.18: Absorption characteristics of a spun film of MEH-PPV, Coumarin 343, metal-free phthalocyanine (H_2Pc), and C_{60} compared with the solar spectrum. The inset indicates the absorption of MEH-PPV/C_{60} only.

the solar spectrum. The AM1.5 best represents the solar spectrum at ground level and can be compared to material absorption spectra for optimal matching. The peaks centered at 670 nm and 700 nm are due to metal-free phthalocyanine (H_2Pc) [37]. Unfortunately MPcs have limited to no solubility in most organic solvents, making the integration of these materials into solution based processing non-trivial. As seen in Figure 1.18, light absorption within the range of H_2Pc is still very limited, and this is a typical problem confronted when attempting to dissolve unsubstituted MPcs in solution. Specific milling and grinding techniques have been developed to aid suspension in various solvents however, obtaining particle sizes below 1 μm is difficult and so electronic properties generally suffer [41].

1.4 Current Challenges

1.4.1 Spectral Overlap

A challenge currently limiting the efficiencies of conjugated polymers is their spectral absorption. While inorganic semiconductors have broad absorption properties, organic materials have sharper and more narrow absorption characteristics. For example, P3HT absorbs strongly only within about a 200 nm range and the same is true for most MPcs and other organics. P3HT has a band gap of 1.9 eV (650 nm) giving it a maximum ability to harvest only 22.4% of incident photons under full illumination [19]. This limit can be slightly improved in a bulk heterojunction, due to the absorption contribution of the acceptor molecule, however this is typically not high and most models do not treat the acceptor as a strong contributor to total current generation [19].

1.5 Methods for Device Enhancement

1.5.1 Buffer Layers

The addition of ultrathin interlayers between the acceptor material and the top contact has been shown to be advantageous [42,43]. Although these layers do not absorb within the visible range or contribute to charge generation, devices incorporating such films show higher efficiencies [44].

A common buffer material used in small molecule OPV cells is 2,9-dimethyl-4,7-diphenyl-1,10-phenanthroline also known as bathocuproine (BCP). BCP, a wide band gap material is an effective exciton blocking layer (EBL) and device improvement has been attributed to improved exciton harvesting in the active layer [44]. As an EBL the layer restricts exciton diffusion and subsequent quenching at the Al electrode [44]. BCP also acts as a diffusion barrier against Al atoms into the acceptor layer, slowing the creation of recombination sites [44]. BCP is thought to be important during the deposition of the metal contact where it acts as a thin protective barrier against acceptor layer damage during metal deposition [43]. It appears that BCP film thicknesses under approximately 10 nm do not affect the charge collection rate and an optimal thickness between 8-10 nm has been reported [43]. Unfortunately, BCP is known to crystallize rather quickly under the presence of moisture, leading to device degradation. The search for an optimal EBL layer is still underway [42, 45].

LiF is another material studied for use as an interlayer in organic photovoltaics. Bulk heterojunction polymer/fullerene solar cells show increases in V_{oc} and FF with the insertion of an ultrathin (1.5 nm) layer of LiF [46]. Although there are a number of ideas as to the basis for improvement, it appears as though the layer forms a dipole moment across the junction due to orientation of the LiF molecules or associated chemical reactions within the film. This dipole effectively shifts the vacuum level offset and modifies the work function of the metal contact [46]. The result is improved charge transfer across the interface and greater PCE [46].

This section has currently only focused only on modification of the top electrode however improving contact between the ITO anode and the active layer has also successfully improved cell performance [47,48], Poly(3,4-ethylenedioxythiophene) poly(styrenesulfonate) or PEDOT:PSS is a doped transparent conducting polymer that is commonly used as a buffer layer in solution-processed OPV. Thin layers of PEDOT:PSS deposited on ITO exhibit several beneficial effects. Improved device performance has been attributed to better selectivity of the electrode, reduced roughness at both the electrode and active layer interface and higher photovoltage via surface enrichment of PSS components [47]. Macroscopically the buffer layer improves J_{sc} and FF considerably in complete devices. Other interlayers such as vanadium oxide (V_2O_5) and molybdenum oxide (MoO_3) can effectively substitute PEDOT:PSS as a buffer layer [48].

Direct ITO modification is a straightforward method of improving device performance and this procedure can be combined with other interlayers for further improvement [49]. UV-ozone treatment and plasma cleaning have been shown to remove any lingering contaminants on the ITO surface remaining after the cleaning procedure. As well, the work function of the electrode also improves [49,50]. Treatment for optimal durations increases the current density in the device, whereas treatment beyond approximately 10 minutes is thought to increase the surface oxygen contaminants such as (O^{2-}, OH^-, organic oxygens and H_2O) [49].

1.5.2 Series Tandem Structures

A successful method for improving device performance and spectral absorption is with series tandem structures [51]. Essentially, tandem structures consist of stacked active layers, each tuned to a region of the spectrum, and separated by a semitransparent interlayer. An example of this concept can be seen in Figure 1.19 where a P3HT/PCBM bulk heterojunction is the primary cell and a CuPc/C_{60} bulk heterojunction is the back cell [52]. Spectral absorption is broadened and voltage is improved considerably in organic series tandem structures. This technology has already been used in niche applications such as space or concentrator cells using inorganic semiconductors [51]. The presence of successful commercial products and record efficiencies shows that this is a viable approach for improving efficiencies. Series tandem structures have also been used in organic PV research with success [52–55]. In OPV the

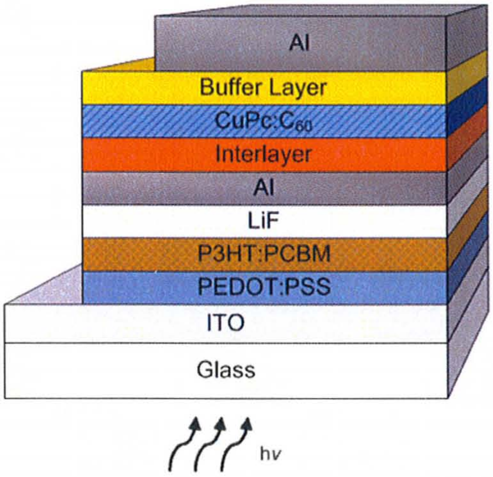

Figure 1.19: Series tandem structure.

highest cell efficiencies have been obtained using series tandem structures. It should be noted that current must be carefully controlled in each layer because J_{sc} is limited by the first or second active layer in the series cell [53].

With careful current matching, V_{oc} can be enhanced considerably, a property that is typically low in OPVs. When making series tandem cells, fabrication procedures can become quite complex, especially in the case of solution-processed cells. The large number of sequentially deposited films can easily become damaged during upper layer deposition, ruining devices. The intercellular layer also causes some energy losses due to light reflection and absorption within the cell.

1.5.3 Parallel Tandem Structures

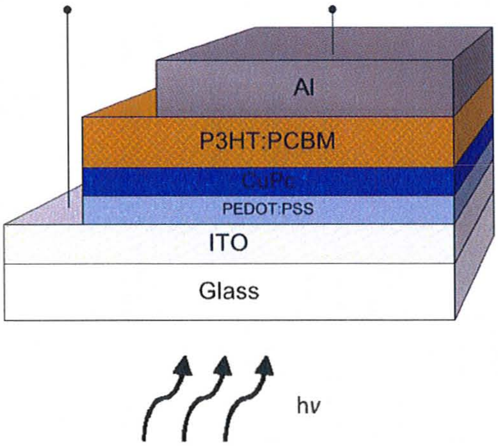

Figure 1.20: Schematic of a simple parallel tandem structure.

Another interesting approach for enhanced light collection and charge generation is a parallel tandem structure [56, 57]. This approach is a more simplified alternative to the series tandem structure and employs a subcell in conjunction with a bulk heterojunction layer without the use of a recombination layer between the two, as in Figure 1.20 [56]. The lack of an interlayer reduces the complexity and the amount of light lost due to reflection or absorption by the semitransparent connecting architecture. Zhang proposed a parallel tandem structure in which PCBM in a bulk heterojunction was also in contact with a CuPc subcell via a bilayer heterojunction [56]. The end result is photoexcitation and charge creation contributions from both subcells and a wider spectral coverage. J_{sc} was found to be additive in the parallel cell. The short circuit current was almost equal to the sum of currents from both a standalone bilayer and bulk heterojunction added together. The efficiency of the combined tandem cell was in fact approximately equal to the combined performance of each standalone subcell.

There are several challenges to achieving efficient parallel tandem structures. Current generated by each subcell should be approximately equal so as to prevent accumulation of photogenerated charges [58]. This entails careful control of each layer thickness. Energy level matching is quite important in this type of structure as well, and ensuring a cascade of available energy levels is important for proper charge collection. The absorption characteristics of each layer also needs to be considered, and only materials with complementary absorption profiles should be matched. In addition, during the fabrication process, upper layers need to be deposited in such a manner that they do not destroy or damage underlying layers. MPcs are generally a good choice because they do not dissolve readily in many organic solvents. This prevents them from washing away during the spinning of upper layers.

1.6 Scope of Research

Using materials expertise at Xerox Research Centre of Canada (XRCC), this research aims to integrate near-IR sensitive materials such as phthalocyanines into new device structures for improved performance and to provide better spectral matching, while retaining the simplicity and elegance necessary for scale-up to larger surfaces and increased production. Expertise in materials synthesis, purification, deposition and characterization at XRCC has been utilized to develop novel structures and devices used to capture greater energy from the sun by way of semiconducting organic materials. Fabrication via solution processing, vacuum deposition and hybrids thereof have been used to attain optimal device structures. Control of MPc thin film properties has been reported in literature and the use of these characteristics from the perspective of photoactivity, mobility, absorption characteristics and charge transport are utilized to the fullest potential in order to attain the greatest efficiency gains.

Chapter 2

Lab Equipment Description

2.1 Vacuum Fabrication

2.1.1 Train Sublimation

For optimal OPV device properties, material purity must be as high as possible [33]. Many of the active layer materials used, such as MPcs and C_{60} are not pure in their purchased or synthesized forms. Small amounts of impurities can lead to difficulties during the deposition process and a drastic reduction in overall device performance. Impure material can degass considerably during deposition, affecting the vacuum, and can erratically eject large amounts of material from the source boat, ruining film quality [33]. Train sublimed MPcs have shown increased photoactivity and improved PV performance following train sublimation [33]. It is important for MPcs to be singly or doubly sublimed in a train sublimation tube before being used in OPV device fabrication.

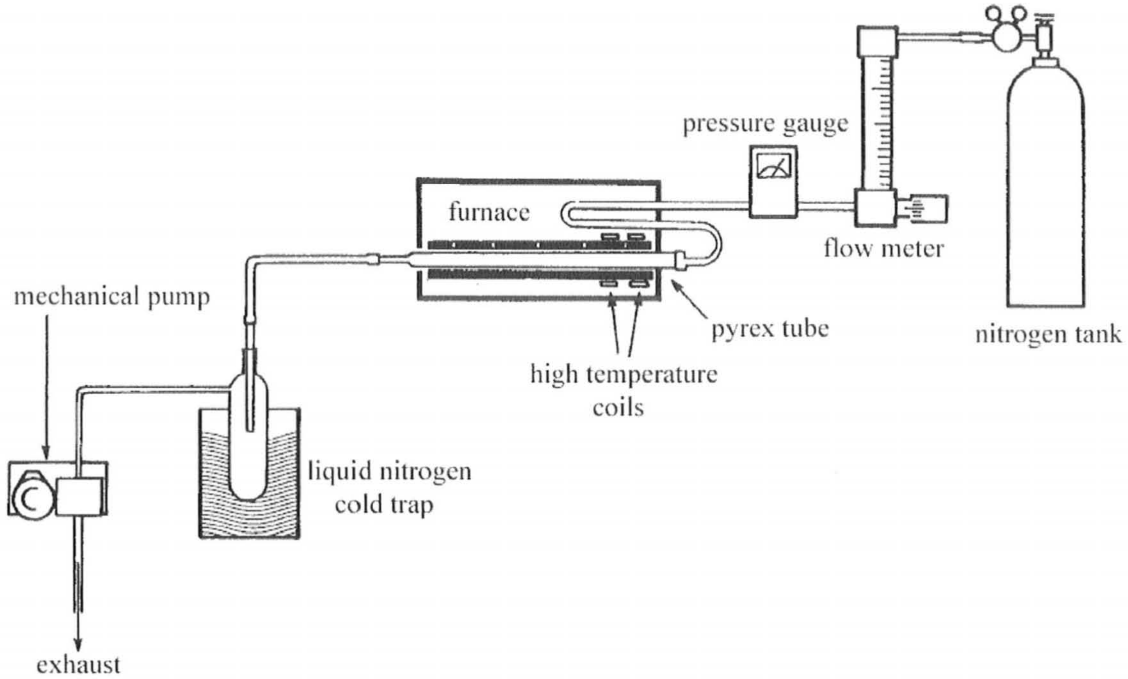

Figure 2.1: Schematic of the train sublimation system

The train sublimation system consists of a long heater tube containing three heating elements connected to thermocouples which control the temperature within each region along the tube. A schematic of the system can be seen in Figure 2.1 [33]. Unpurified material is placed into a long glass tube and the tube is then placed inside the furnace. A slight vacuum is maintained on the system and monitored by a pressure gauge. N_2 gas flow is then initiated and maintained throughout the process and is used to transport sublimed material along the tube where it can deposit on the tube surface in a cooler zone. The high temperature zone is maintained at a level near the sublimation point of the material for the duration of the process, and decreases approximately linearly along the length of the tube. In the case of MPcs this is around 550 °C and for C_{60} about 570 °C. Sublimation is allowed to proceed for over 12 hrs and upon completion the tube is slowly cooled and the material collected.

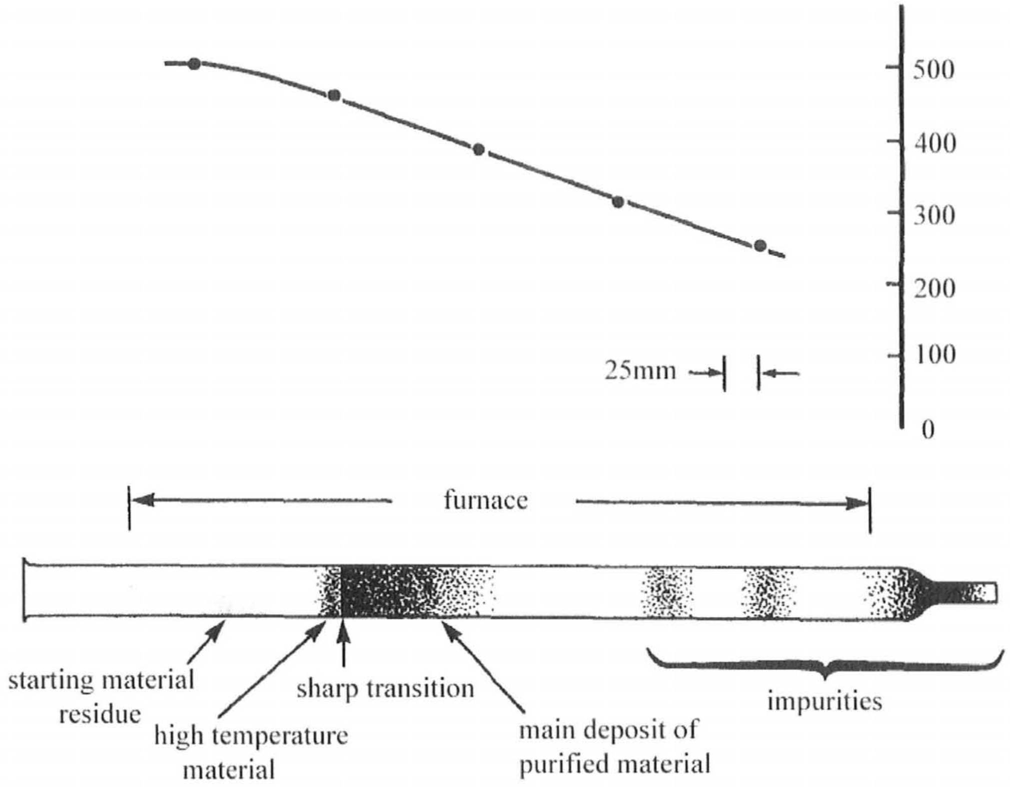

Figure 2.2: Temperature distribution and typical deposition zones following the sublimation process.

There are a five distinct zones of deposited material along the tube after sublimation as seen in Figure 2.2 [33]. The leftmost region consists of residue left behind from the starting unpurified material. This is typically a black fluffy ash-like powder of low density. Purified MPc forms two zones, a light coloured amorphous material adjacent to the high temperature zone and, followed by a sharp transition, a larger region of dark crystalline material. In the case of C_{60} purification, the high temperature amorphous zone does not appear to be present. Further along the tube several sharp zones of impurities are typically found and these regions are generally yellow or brownish in colour and contain more volatile materials with a lower sublimation temperature. The amount of these materials deposited depends heavily on the quality of the starting material and the material supplier. Further, the system contains a liquid nitrogen cooled cold-trap to capture any remaining impurities that pass through the tube undeposited, preventing volatiles from damaging the mechanical vacuum pump. The volatile impurities are likely the cause of outgassing and unstable deposition rates when unpurified material is used in the vacuum chamber during device fabrication.

The material harvested and used in device fabrication is the darker crystalline deposit with adequate quantity for use in a variety of experiments. The high temperature material is only present in very limited quantities and was collected but not studied in detail.

Train sublimed materials show improvement in a range of attributes. Purified materials show better deposition behaviour and rarely *puff* material from the boat into the chamber. *Puffing* describes the ejection of large amounts of unsublimed material from the heated boat into the chamber and usually results in unusable films for devices. This was especially a concern with MgPc and ZnPc where this behaviour is more common. Outgassing is also considerably reduced by train sublimation, saving time and ensuring deposition under low vacuum. Ultimately, train sublimation results in improved OPV device characteristics [59].

2.1.2 Vacuum Chamber

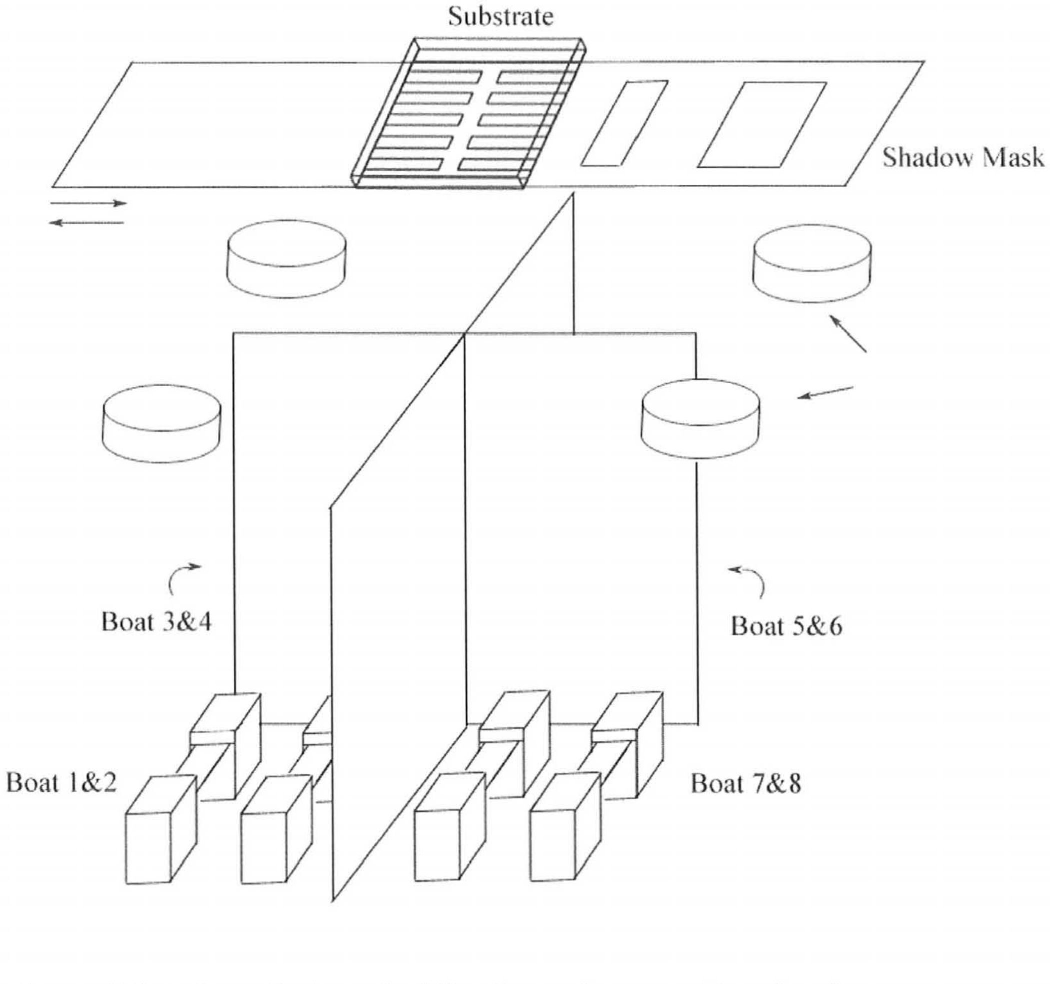

Figure 2.3: Schematic layout of the thermal evaporation chamber.

A vacuum chamber equipped with a CTI-Cryogenics Cryo-Torr cryopump was used for thermal deposition of the majority of thin films. Only the Al layer in solution-processed devices was deposited by a different evaporation system described in Section 2.2.3 A diagram of the chamber layout can be seen in Figure 2.3. The vacuum chamber housed eight boats with four sources allowing complete fabrication of evaporated cells without breaking vacuum. A movable mask could be controlled from outside the chamber, giving complete control over device structure during deposition. Chamber pressure was monitored using a Granville-Phillips Micro-Ion Plus and all evaporations occurred at pressures below 5.4×10^{-4} Pa. Film thickness was monitored with quartz crystal oscillators, measuring changes in the oscillating frequency of the crystal as thickness of deposited material increased. Each monitor had a measured correction factor associated with the geometry of the vacuum chamber and accounted for material density. Deposition was controlled by an Inficon IC/5 Deposition Controller. A shutter precisely controlled the exposure time of the substrate to the heated material and allowed for film deposition only during periods of steady film deposition rates.

Since the thermal evaporator contained multiple sources, simultaneous evaporation of two materials could be controlled. Multiple boats could be heated together to a controlled deposition rate and the shutter then opened. Each source was monitored by its own quartz crystal, allowing individual control of deposition rates of both materials.

In the case of organic materials, especially MPcs that have not been thoroughly purified, there may be significant outgassing during initial heating. Outgassing raises the pressure in the chamber considerably which therefore must be allowed to fall before material deposition onto the substrate. Multiple purification runs in the train sublimation tube reduced the likelihood of outgassing and puffing however there was always a small chance of sudden material ejection during any deposition. Puffing was more likely when the boat was initially packed with new material or when near the very end of material in the boat, when small amounts of char could also be present.

2.2 Solution Processing

2.2.1 Glovebox

Active layers of solution-processed solar cells were spun within a glovebox. The glovebox provided an inert environment to perform spinning and annealing activities during cell fabrication since oxygen and humidity are known to speed the degradation of organic PV cells. Desiccant was used to keep humidity levels below 1.0% measured with a Omega OM-PLTH Temperature and Humidity data logger during fabrication, and nitrogen was continually flushed through the glovebox to reduce oxygen levels below 0.5% measured with an MSA Altair O_2 Pro during spinning. The glovebox also housed a hotplate, allowing controlled annealing during fabrication. Annealing was typically used after deposition of the initial PEDOT:PSS layer to bake off any remaining water, and after cathode deposition in the case of cells containing P3HT.

2.2.2 Spin Coater

PEDOT:PSS layers were spun using a Specialty Coating Systems Spincoater Model P6700 Series in a fumehood. PEDOT:PSS was not deposited inside the glovebox because the polymer is typically dissolved in water and would lead to contamination of the glovebox with water vapour. Exposure to oxygen during and following

PEDOT:PSS deposition appears to have a negligible effect on the initial layer and subsequent device performance.

A Specialty Coating Systems G3-8 Spincoat was used to spin the active layer of PV cells and was located inside the glovebox.

2.2.3 Bell-Jar Evaporator

An Edwards Coating System E306A bell-jar evaporator was used to deposit the cathode during solution-processed cell fabrication. A vacuum of 2×10^{-3} Pa was reached before deposition of the metal layer. This evaporator only had a single source however due to the smaller chamber size, pump-down times were much shorter and reduced the time needed to complete the devices following active layer deposition. This is important when considering the fast decay times of OPV devices.

2.3 Characterization

2.3.1 *J-V* Measurements

Completed devices were placed in an in-house designed sample holder. The sample holder used a circular shadow mask with an active area of 7mm^2 on each device. Devices were illuminated through the ITO electrode and electrical contact was made with pressure contacts. The sample holder allowed the connection of a gas line, and was used to flush nitrogen into the holder while measurements were taken. This reduced the rate of degradation by keeping the cell in an inert environment.

An Oriel 96000 solar simulator with an AM1.5G spectral filter was used to simulate the solar spectrum, and was calibrated to 100 mW/cm^2 using a Newport 818-UV/CM detector and Newport 1830-C optical power meter. I-V characteristics were measured using a Keithley 238 source-measure unit. A computer collected the output I-V data.

Spectral filters were also placed between the Xenon arc lamp and the device to measure I-V curves of particular segments of the solar spectrum. Several MPcs have sensitivity extending into the infrared, so filters allowing only long wavelengths beyond 650 nm through were used for partial spectral analysis, in conjunction with full spectral data. Cut-off filters allowed measurement of current generated at all wavelengths above or below certain wavelengths. Filters such as ll650 (permitting only wavelengths longer than 650 nm) and ll700 (only wavelengths above 700 nm) were often used to determine proof of concept in new structures and to decide if further analysis using EQE measurements should be performed on a particular device. The following section describes the EQE setup and measurement procedure.

2.3.2 External Quantum Efficiency

EQE measurements were taken using a calibrated Photon Technology International monochromator. Calibration was performed using a Newport 818-UV/CM detector and Newport 1830-C optical power meter by measuring power at each wavelength. A Keithley 6485 picoammeter measured short circuit current as a function of wavelength in the PV device. The measured current from the device was compared to the incident photons at each wavelength to generate a response curve across a given range.

2.3.3 UV-vis Measurements

Optical absorption spectra were measured using a Cary 5000 UV-vis-NIR Spectrometer by Varian. The baseline absorption of the substrate was subtracted from all measured curves presented in this document. In most cases UV-visible curves have been normalized to aid comparison of absorption characteristics and eliminate any variability in film thickness.

2.3.4 Profilometer

Film thicknesses were measured using a Digital Instruments Dektak 6M Programmable Surface Profilometer. A small needle head was used to determine elevation along a straight line through samples. For each thickness value, several measurements were taken and an average thickness was determined.

Chapter 3

Experimental

3.1 Conducting Substrate Etching

50 mm × 50 mm Indium-Tin-Oxide (ITO) coated aluminosilicate glass slides were purchased from Delta Technologies and used in device fabrication. ITO slides were etched in-house to create patterned conducting areas on the glass. Two ground pads and ten fingers were etched on the surface, separated by insulating glass as seen in Figure 3.1.

Etching was performed using a procedure developed in-house. The procedure consisted of spinning AZ-1518 positive photoresist at 2500 rpm for 60 s onto a cleaned ITO substrate, followed by soft baking and then UV exposure through a mask. The mask pattern matched the final pattern seen in Figure 3.1. The photoresist was then developed in the MR-314 developer and rinsed, followed by hard baking in an oven. The ITO was etched in a mixture of hydrochloric (HCl) and nitric (HNO_3) acid to

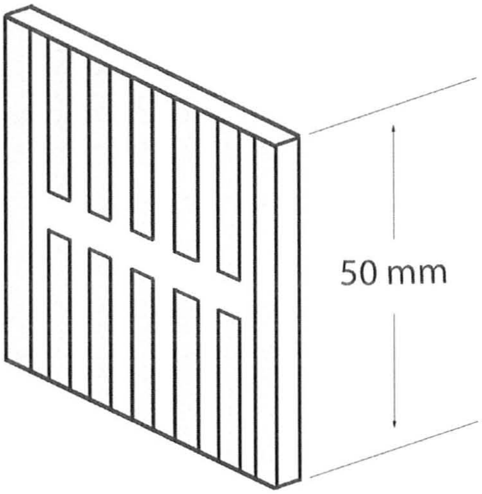

Figure 3.1: Etched indium-tin-oxide (ITO) conducting surface on glass

pattern the substrate. The final step consisted of removing any remaining photoresist using acetone. Etched ITO slides were used for both solution-processed and vacuum coated devices.

3.2 Substrate Cleaning Procedure

The cleaning procedure for etched ITO slides consisted of a series of steps designed in house. The importance of an exceptionally clean substrate is tantamount in device fabrication, and can be the grounds for the disparity between a shorted device and one with optimal photovoltaic performance. Dust can hinder cell performance by disrupting film quality and by causing physical shunts through the thickness of the device. Other organic materials can reduce device performance by affecting the work function of the electrode or preventing optimal contact between the initial layers and the ITO [49]. The nature of the nanometer thicknesses of films required utmost cleanliness of substrates. Since fabrication was in a traditional lab setting, dust was managed as best as possible by transporting substrates inverted, and keeping them constantly covered when the conducting side faced upwards. The preliminary ITO cleaning procedure differs only slightly between solution-processed and vacuum deposition. Solution-processed cells included an additional step involving plasma cleaning of the ITO surface before spinning the first film. The cleaning procedure employed is as follows:

1. Place the etched ITO slides in a soap solution (4 mL Extran for each 200 mL of DI water) and soak for at least one hour. The slide is ready for the next step when water wets the surface well and does not bead.
2. Scrub the slides using a kimwipe and the soap solution.
3. Run hot water over the surface for several minutes to remove all soap solution. Any remaining soap will ruin the device.
4. Rinse the slides sequentially with DI water, methanol, and then isopropanol.
5. Suspend the slide above boiling isopropanol for 15 minutes in a beaker.
6. Move the covered slides to an oven to dry completely at temperatures above 140 C for 20 minutes.
7. UV-ozone clean the slides for 10 minutes.
8. (Solution processing) Plasma clean the surface before spin coating the first layer.

3.3 Improved Spectral Coverage with Integration of MPc

3.3.1 PIN Diode (Top MPc)

3.3.1.1 Justification

Solution-processed P3HT and PCBM bulk heterojunction solar cells have strong optical absorption from 300 nm to 650 nm. Above 650 nm, absorption is negligible and since a large portion of solar energy resides above this, it would be advantageous to find a means of absorption and charge generation within this region. Since MPcs typically have strong absorption peaks in the near-IR region of visible light, incorporating them into organic photovoltaic devices could potentially broaden absorption and improve PCE.

Ideally, integrating MPcs directly into solution-processed fabrication would be simplest; creating an active layer bulk heterojunction of P3HT, PCBM and MPc. Unfortunately dispersing MPcs into solution is not elementary and all cells we have fabricated using this approach had poor photovoltaic response. MPcs have only limited solubility in a few organic solvents, and are generally only soluble to meaningful levels in acids [41]. Grinding and milling methods have been developed to attain small particle size and temporary dispersions in some solvents however milling times as long as several days may be required. Damage to any co-dissolved conjugated polymer materials during this processing is a concern, as well as the likelihood of contamination from the metal or glass bead milling material. MPcs typically form long crystals consisting of columnar packing of a stack of phthalocyanine particles, and all central metal atoms aligned. This leaves the edges quite unreactive, as only C-H bonds appear at the periphery of the molecular ring system in a phthalocyanine molecule [21,29]. Some success in dissolving MPcs has been made with modification to the phthalocyanine ring systems, allowing for direct use in solution-processing, however current generated at higher wavelengths is quite low using this technique, so finding an improved method is warranted [39,60].

3.3.1.2 Structure

A novel *p*-i-*n* (PIN) structure provides an alternative to molecular modification of the MPc, and does not require the development of a specific procedure for dispersing each MPc moiety in liquid solvent. Each MPc has unique dissolution requirements, making it necessary to have a different procedure for suspending each species.

The respective *p*-i-*n* layers are deposited sequentially and form the *p*-transport layer, intrinsic layer and *n*-transport layers. In traditional PIN devices the *p* and *n* layers are created using doped wide band gap materials, with only the intrinsic layer absorbing visible light. The interface at each opposing side of the intrinsic layer acts as a filter, only allowing the correct type of charge carriers to leave. This is accomplished by careful energy level matching, achieving the correct bias. Figure 3.2 shows the general structure and energy level positioning of a PIN cell. In the case of this study, unlike in other organic PIN structures, the *p* and *n* wide-gap layers have been left undoped [61–63]. In organics doping has been achieved by co-evaporating other materials with the *p* and *n* type layers to improve conductivity and reduce

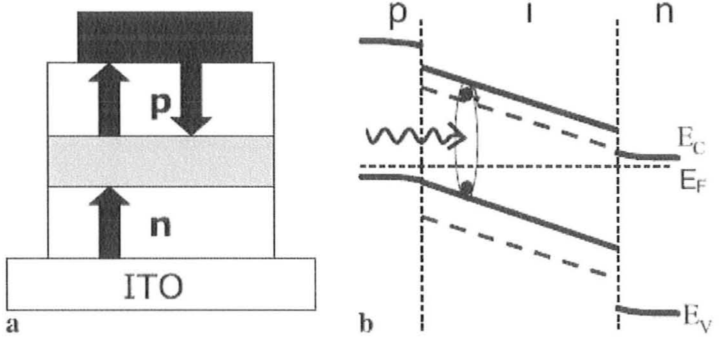

Figure 3.2: a) General PIN-type solar cell structure. The intrinsic region is located between *p* and *n* type materials. b) Energy diagram of a general PIN-type solar cell with a bulk heterojunction intrinsic region.

ohmic losses in the device, however this is not within the scope of this study [61].

In this study the *i* photoactive layer is actually a hybrid structure consisting of an MPc:C_{60} mixture in a 1:1 ratio, sandwiched between the *p* and *n* type materials. The *p* material used is P3HT whereas the *n* material is C_{60}. This structure essentially couples an MPc:C_{60} bulk heterojunction with P3HT. The device architecture is depicted in Figure 3.3 and following PEDOT:PSS and P3HT spinning, entails the evaporation of an MPc:C_{60} layer on top. A thin layer of C_{60} is then vacuum deposited prior to the aluminum cathode.

It should be expected that there will be strong absorption by the P3HT film and some by C_{60} film as they both have absorption characteristics within the visible spectrum. Integrating an MPc layer improves total coverage because the spectra is complementary to the other two materials. Figure 3.4 indicates the absorption

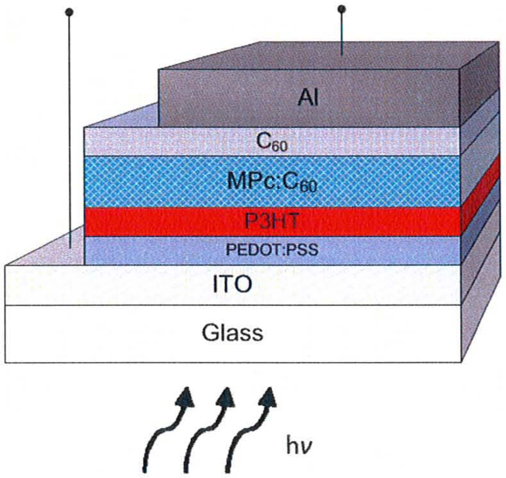

Figure 3.3: PIN-type device structure.

profiles of the two strongly absorbing materials in their pristine state. The interface between the P3HT and $MPc:C_{60}$ allows for charge separation of excitons formed in the P3HT film.

Energy levels of the device structure should match in order to attain optimal cell characteristics. An energy diagram for the device is shown in Figure 3.5. Suitable energy level matching suppresses minority charge carriers with energy barriers and creates a cascade of available energies, allowing charges to travel to their respective electrodes. There is a suitable range of HOMOs and LUMOs that the intrinsic layer material can have, given the other two. The HOMO and LUMO of C_{60} are 6.1 eV and 4.5 eV and for P3HT, they are 5.2 eV and 3.5 eV respectively. The energy diagram in Figure 3.5 below depicts these two windows of allowed energy levels for the material. The HOMO must lie between 6.1 eV and 5.2 eV while the LUMO must lie between 4.5

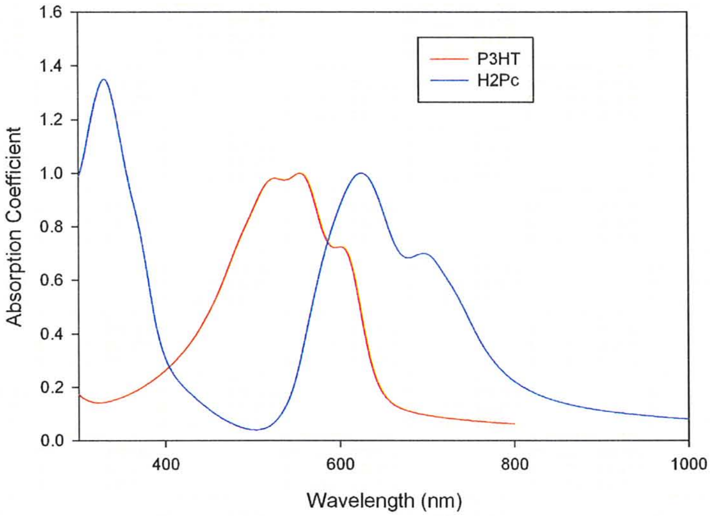

Figure 3.4: Absorption profiles of materials used in the PIN-type solar cell.

eV and 3.5 eV. Fortunately MPcs typically have HOMOs and LUMOs close to these values. A table indicating energy levels for a variety of MPcs is shown in Table 3.1. Note that there is some error in the measurement of HOMO and LUMO parameters and this can be as high as several tenths of an eV.

The device was fabricated by spin coating PEDOT:PSS in a ratio of 3:2 with water onto the ITO coated slide at 1000 rpm. This resulted in films approximately 30 nm thick, and was followed by annealing on a hotplate in the glovebox at 120 °C. After annealing of the PEDOT:PSS, a layer of P3HT was spun on top at 1000 rpm from a 20 mg/ml solution in (1,2)dichlorobenzene. The sample was then transferred to a vacuum evaporator and put under a vacuum of 5×10^{-4} Pa before deposition of the final layers. A 20 nm (1:1) layer of H_2Pc:C_{60} was deposited, then 20 nm of

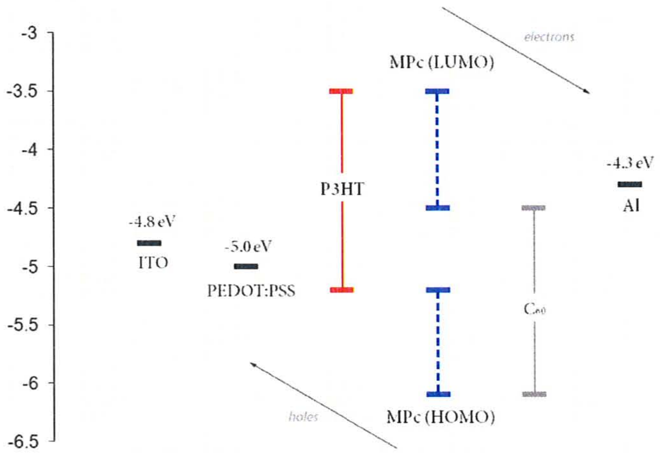

Figure 3.5: Energy diagram for the proposed PIN-type structure.

C_{60}, followed by a 50 nm Al cathode. The device was then annealed at 140 °C for 10 minutes before testing. Literature indicates that the HOMO and LUMO of H_2Pc should fall within the allowed energy levels of the structure incorporating P3HT and C_{60}.

3.3.1.3 Experimental Results

Devices were illuminated with 100 mW/cm^2 simulated sunlight through the ITO electrode, using an Oriel 96000 solar simulator with an AM1.5G spectral filter. The active device area was 7 mm^2 defined by a shadow mask. Input power was monitored with a Newport 818-UV/CM detector and Newport 1830-C optical power meter. A Keithley 238 source-measure unit collected output data.

J-*V* response curves of devices with structure shown in Figure 3.3 using H_2Pc in the MPc:C_{60} layer were measured under full illumination and a power conversion

Table 3.1: Energy Levels of Various MPcs.

MPc	HOMO	LUMO	Reference
H_2Pc	5.2	3.5	[64,65]
CuPc	5.3	3.6	[66]
ZnPc	5.2-5.3	3.3-3.8	[67,68]
MgPc	5.4	3.9	[69]
ClAlPc	5.0	*	[64]
ClGaPc	*	*	
ClInPc	5.1	3.5	[70]
TiOPc	5.7	4.0	[71,72]
VOPc	5.6	4.2-4.7	[73,74]

* denotes no data

efficiency (PCE) of 0.76% was reached, as seen in Figure 3.6. Compared to a baseline P3HT:PCBM cell with PCE of 2.08%, the efficiency is lower. The V_{oc} of the baseline cell is 0.57 V and the J_{sc} is 8.1 mA/cm^2 whereas for the H_2Pc cell the V_{oc} and J_{sc} are 0.39 V and 3.2 mA/cm^2 respectively. The FF however did improve, going from 45.4% in the baseline cell to 61.7% in the H_2Pc PIN cell. Devices with a simple P3HT/C_{60} bilayer heterojunction showed no noticeable photovoltaic behaviour.

Poor performance is most likely due to the P3HT layer being too thick. Photogenerated excitons can only dissociate into free charges when they are created within the average diffusion length from the heterojunction. Organic materials tend to have low mobilities, leading to diffusion lengths on the order of tens of nanometers [7]. In the P3HT layer there is very limited dissociation far from interface with MPc:C_{60}. Since the spun layer is approximately 40 nm, any photogenerated species greater than the diffusion length away from the interface will recombine and cannot contribute to overall current. This region, being the first which incident light impinges on, will

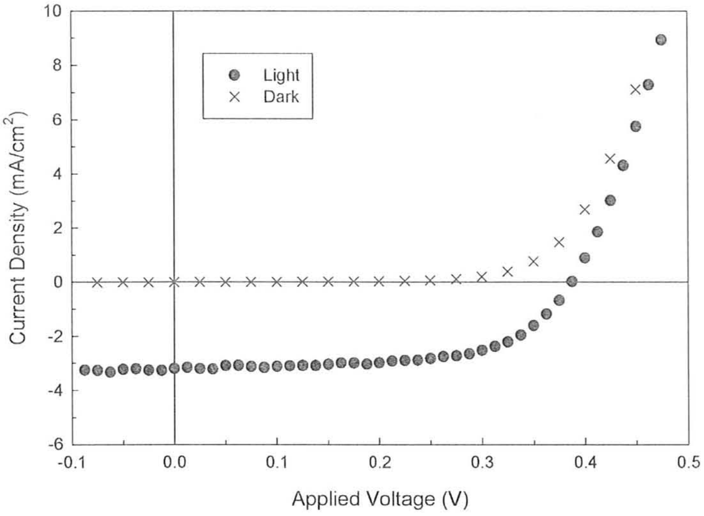

Figure 3.6: *J*-*V* response curve for a PIN-type photovoltaic cell incorporating H_2Pc.

also absorb light and reduce the available photon energy to subsequent layers where charge could have been generated, further reducing cell performance.

This structure shows that a pure P3HT layer can contribute to charge generation and cell efficiency when an MPc is connected via a heterojunction. Device optimization including a reduction of the thickness of the P3HT could improve cell efficiency, bringing properties closer to that of a baseline P3HT:PCBM bulk-heterojunction.

3.3.1.4 Future Work

This structure likely suffered from the pristine P3HT film being too thick since the layer thickness was much greater than the P3HT diffusion length. This likely led to higher recombination rates, causing a reduction in J_{sc}. Reducing P3HT layer thickness could improve device efficiency considerably. This can be achieved by spinning a lower concentration of P3HT, or by increasing spinning speed during deposition. Another avenue for further study is to test a variety of MPcs in the place of the H_2Pc. The number of MPcs available offers the possibility of discovering a material superior to that of the H_2Pc.

Further, annealing tests can be performed to determine if annealing before MPc deposition can lead to improved device performance. This would eliminate exposure of the MPc film to high temperatures, potentially reducing the chance of affecting film properties due to interactions with other layers. In some cases, when annealing completed devices with MPc layers already evaporated, the formation of large regions of a new phase could be observed under an optical microscope. This new phase and its effect on device properties could also be further studied.

3.3.2 Bottom MPc Tandem with PQT-12

3.3.2.1 Justification

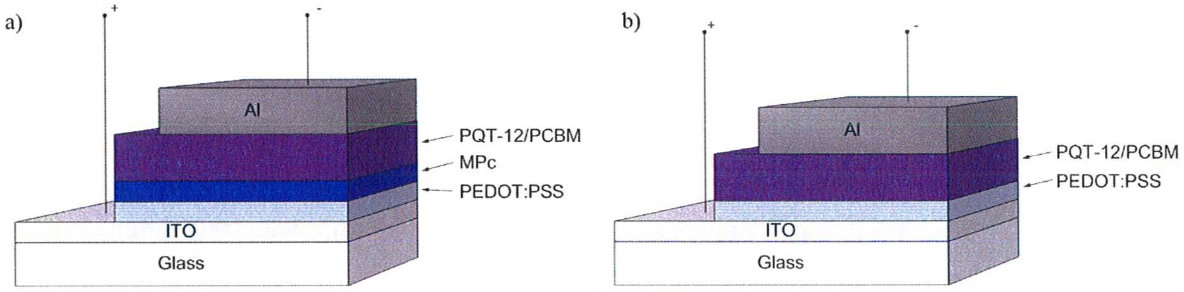

Figure 3.7: Device structure of a) the multilayer cell with MPc and b) the control cell.

Spectral coverage improvement has been attempted in a number of ways, including the use of low band gap polymers, tandem cells, and small molecules [37,39, 53,56,75–80]. Designing tandem structures by stacking has been shown to be effective at enhancing spectral coverage [53,56]. Combining or stacking multiple materials of complementary absorption profiles can improve characteristics of organic PV devices without the need for an intercellular connection layer [56]. MPcs are a group of small molecules with Q-band absorption in the red to near-IR ranges, complementing the absorption of PQT-12 and PCBM. Solvent damage can occur to underlying layers when spin coating multiple solution-processed films, so this must be accounted for when selecting an appropriate processing method. Furthermore, design of effective multilayered cells involves careful control of layer thickness to match the short circuit current density (J_{sc}) of each subcell, preventing accumulation of photogenerated charges [58]. In this study we investigated the integration of a variety of different MPc films into a PQT-12/PCBM bulk-heterojunction cell for improved performance and spectral coverage.

3.3.2.2 Structure

The device structure is shown in Figure 3.7, indicating both the multilayer cell and the control cell. Devices were prepared on patterned indium tin oxide (ITO) ($\sim$15 $\Omega/\square$) coated aluminosilicate glass, 50 mm × 50 mm substrates. Water soluble poly(3,4-ethylenedioxythiophene):poly(styrene-sulfonic acid) (PEDOT:PSS) was spun onto cleaned substrates at 1000 rpm to form a $\sim$ 30 nm layer. The sample was annealed at 120 °C for 20 minutes in a low O_2 (<2.0%) low humidity (<1.0%)

glovebox. Substrates were then transferred to a cryopump equipped thermal evaporator and a vacuum of 5×10^{-4} Pa was reached before MPc deposition. Quartz crystal monitors were used to control layer thickness. A 16 nm layer of MPc was deposited and a range of central moieties (M) were examined. Monovalent (metal-free H_2), divalent (Cu), trivalent (Al-Cl, Ga-Cl, In-Cl) and tetravalent (Ti=O, V=O) MPcs were used, resulting in seven samples of the same structure but different MPc layer. Each sample also contained a control cell with no MPc. Following evaporation of MPc layers, devices were transferred back to the glovebox where a 20 mg/ml at 15 wt% PQT-12, 85 wt% PCBM solution dissolved in (1,2)dichlorobenzene was spun at 1000 rpm for 60 s, forming a layer approximately 50 nm thick [15]. The aluminum cathode was evaporated at a pressure below 2×10^{-3} Pa.

J-V curves were measured by illuminating the devices through the ITO electrode with 100 mW/cm^2 simulated sunlight using an Oriel 96000 solar simulator with an AM1.5G spectral filter. Input power was monitored with a Newport 818-UV/CM detector and Newport 1830-C optical power meter. A Keithley 238 source-measure unit and PC collected output data. Active device areas were 7 mm^2 defined by a shadow mask. EQE measurements were acquired using a calibrated monochromator (Photon Technology International) and a picoammeter (Keithley 6485) measuring short circuit current as a function of incident light wavelength.

The *J-V* characteristics for the seven MPcs are shown in Figure 3.8. Current densities were calculated by dividing the current by the active area. In all cases the V_{oc} of samples incorporating an MPc layer show improvement over the control.

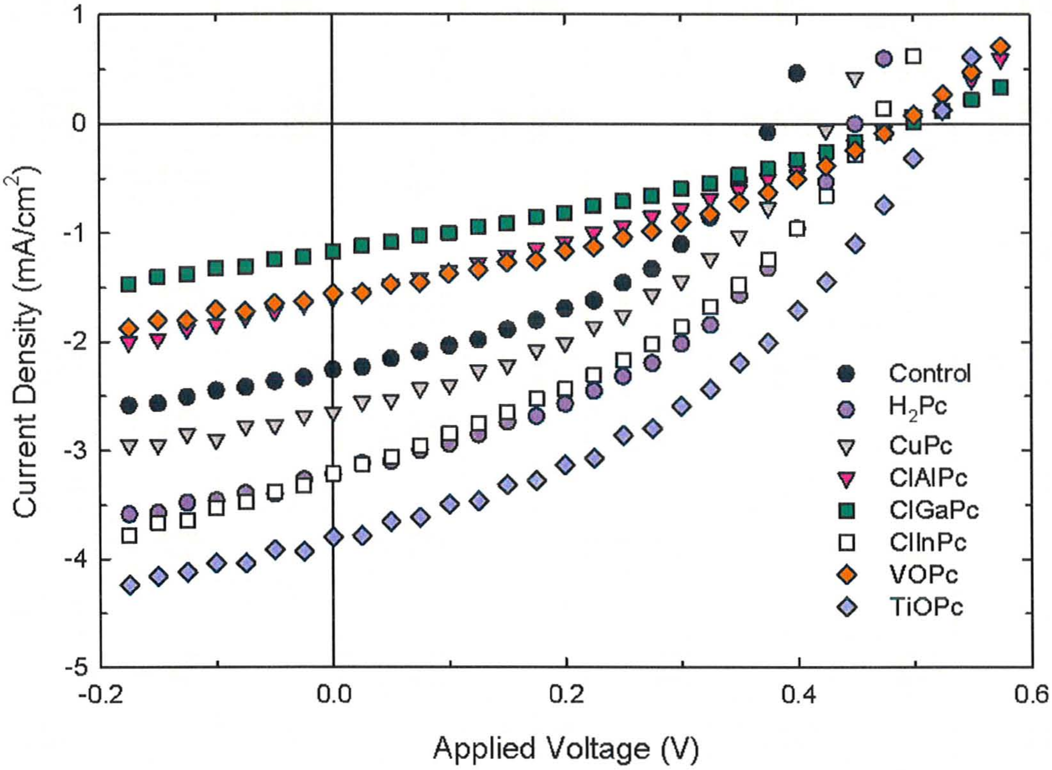

Figure 3.8: *J*-*V* response curves of devices incorporating various MPcs.

The increase in V$_{oc}$ can be attributed to improved energy level positioning, as the lower HOMO of the MPc increases the energy level difference from the LUMO of the PCBM [81]. The highest V$_{oc}$ is attained in the trivalent and tetravalent MPcs. The J$_{sc}$ shows improvement in the CuPc, ClInPc, H$_2$Pc and TiOPc samples. Devices with improved J$_{sc}$ have similar *J*-*V* curve shapes as the control, showing minimal decrease in fill factor. The three MPcs with reduced cell performance (ClAlPc, ClGaPc and VOPc) show a lower slope at the V$_{oc}$. This is indicative of a higher series resistance causing reduced performance. All MPc devices show a reduction in fill factor, and

Table 3.2: *J*-*V* parameters for different MPc layers.

MPc	**V_{OC}(V)**	**J_{sc}mA/cm^2**	**FF (%)**	**PCE**
Control	0.38	2.26	43	0.37%
H_2Pc	0.45	3.22	42	0.61%
CuPc	0.43	2.65	39	0.44%
ClAlPc	0.49	1.60	30	0.24%
ClGaPc	0.50	1.17	31	0.30%
ClInPc	0.47	3.21	37	0.56%
VOPc	0.49	1.79	36	0.31%
TiOPc	0.52	3.80	40	0.79%

this can be explained by the additional series resistance and device thickness versus the control cell. The higher series resistance is likely due to layer thickness being considerably greater than the exciton diffusion length in these MPcs. Since transport properties depend on the moiety of the MPc and MPc layer thickness has been held constant, devices are not necessarily optimized for each MPc. There is potential for improving cell performance by tailoring the MPc film thickness. Further investigation of TiOPc devices has been performed to explain the superior performance obtained in this structure.

When comparing the efficiency of the PQT-12/PCBM control cell to that of a P3HT/PCBM cell, the efficiency of the PQT-12 based cell is noticeably lower. We have found some potential causes for this difference, most notably the morphology appears to be a critical factor. Optimal ratios of PQT-12:PCBM have been found to be 15:85, well below the near 50:50 ratio typical of P3HT:PCBM [15]. Although absorption characteristics and hole mobilities are nearly identical, PQT-12 forms crystalline particles when in solution, making electrical connections poor when spun

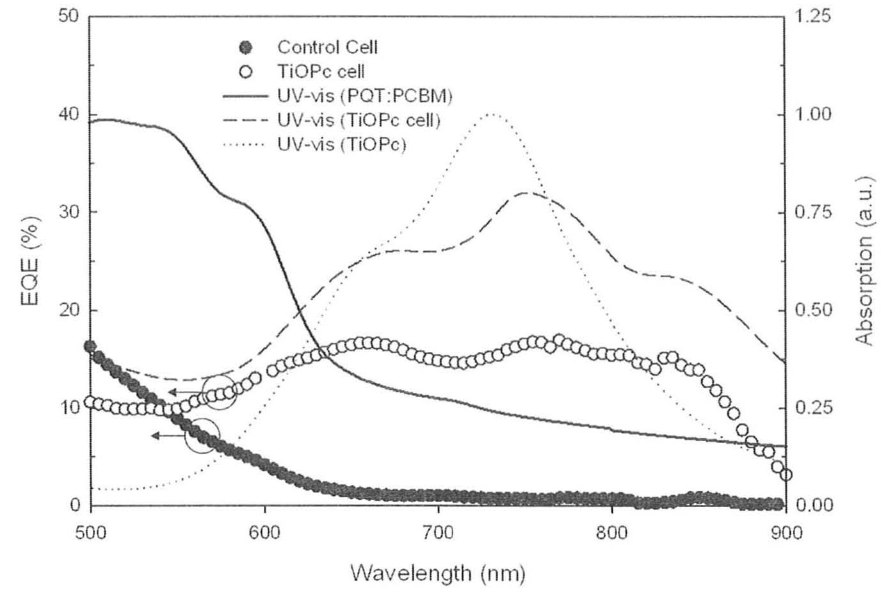

Figure 3.9: EQE of control cell and a 16 nm TiOPc interlayer tandem cell. UV-visible absorption of pristine TiOPc, PQT-12:PCBM and TiOPc device with cathode removed.

as films [82]. We attempted to mitigate this by keeping the solution temperature raised during the entire deposition process, including heated substrates and pipettes however no improvement in efficiency could be gained. Also, due to the morphological challenges with PQT-12/PCBM bulk heterojunction devices, thermal annealing of completed devices does not improve electronic properties, but instead causes phase separation on a micrometer scale, in effect hindering device properties [82]. The macroscopic phase separation forms isolated regions of a single phase on a scale much larger than the diffusion length of any photoexcited state, leading to considerably reduced PCE.

Further investigation of TiOPc devices has been performed to explain the superior performance obtained in this structure. MPcs are known to form a variety of polymorphs via controlled deposition, annealing, or solvent treatment [21, 83–91]. Polymorphism is common in MPcs because intermolecular forces between molecules are relatively weak, allowing for a variety of stacking orientations [21]. As can be seen in the UV-vis absorption curves in Figure 3.9, the near-IR TiOPc absorption peak red-shifts from 730 nm to 750 nm. The pristine TiOPc film corresponds to the typical amorphous absorption profile of TiOPc, consisting of a (not shown) Soret band at 354 nm and a Q-band main peak at 730 nm, with a shoulder centered at 660 nm. There is a noticeable broadening of the absorption to IR wavelengths upon the spinning of upper layers. A shoulder appears above 850 nm in the tandem cell absorption profile that is clearly not attributable to either the PQT-12 or PCBM.

EQE shown in Figure 3.9 gives further insight into absorption and free charge generation at longer wavelengths. The EQE curves closely match the shape of the absorption profile for both the control device and the device with TiOPc. The TiOPc device shows an extension of current generation to higher wavelengths, up to 900 nm. EQE values of 16% are reached within this range, compared to the minimal currents generated in the control sample. The additional current generated at higher wavelengths explains the increase in J_{sc}. The absorption red-shift and evolution of an IR shoulder in the tandem cell UV-vis can be attributed to a polymorph change during contact between (1,2)dichlorobenzene and TiOPc upon spinning of the upper PQT-12:PCBM layer. Since the upper layer is spun directly onto the MPc layer, there is direct interaction between solvent and MPc for the period of time between the dropping of the solution and commencement of spinning. This contact allows for relaxation and molecular reorientation within the MPc film. TiOPc films exposed solely to (1,2)dichlorobenzene solvent containing no PQT-12 or PCBM showed similar shifts in absorption spectra. Direct contact with solvent liquid has been shown to reorient crystal structures of MPc [88, 89]. Crystalline forms of TiOPc should have higher photosensitivity and improved transport properties due to a greater degree of molecular order. At the very least, in this study partial polymorph conversion appears to occur on the order of seconds during solvent exposure. A more complete conversion from Phase I to Phase II TiOPc has been reported after a prolonged exposure to chloroform [87].

A range of TiOPc thicknesses were tested using this device structure to find an optimal layer thickness. All other aspects of the device structure were the same, including PEDOT:PSS film thickness and PQT-12/PCBM solution composition. TiOPc film thickness was varied from 0 nm to 25 nm using a shadow mask on the same substrate. This allowed for an accurate comparison between device properties, as all other layers were deposited with identical conditions. Inter-device variability was controlled using this method. The shadow mask defined five different thicknesses of TiOPc, 0 nm, 10 nm, 15 nm, 20 nm and 25 nm, creating two devices with each thickness. I-V curves indicating the performance of each pair of devices are shown in Figure 3.10. Optimal TiOPc thickness appears to be between 20 nm and 25 nm. J_{sc}, V_{oc} and PCE peak near 20 nm. All three performance parameters indicate optimal thickness lying between 20 nm and 25 nm, slightly thicker than the standardized 16 nm used in this study. This thickness is slightly more than three times the exciton

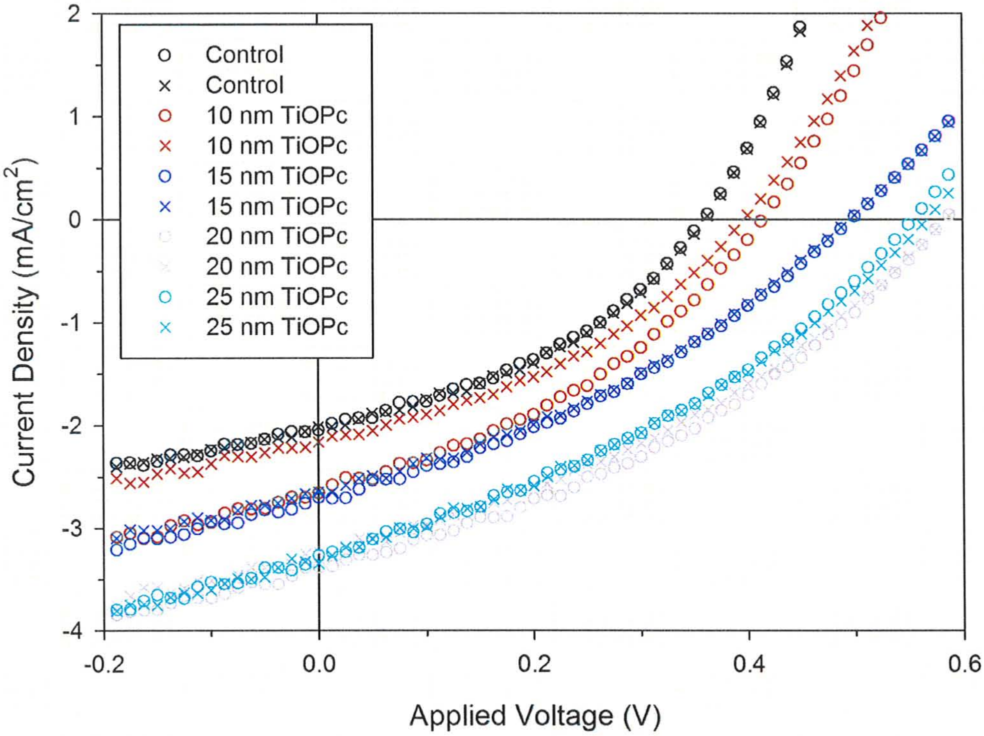

Figure 3.10: I-V curves for a range of thicknesses of TiOPc.

diffusion length in TiOPc [92]. This thickness is similar to the optimal ranges found in other PV structures incorporating a pristine layer of TiOPc [87]. Incorporating an optimal thickness of between 20 and 25 nm could further increase, V_{oc} by 16%, J_{sc} by 23% and PCE by 50%.

Figure 3.11 shows the EQE curves of different TiOPc thicknesses, indicating that the increased J_{sc} is due entirely to current generated at higher wavelengths above 550 nm. The discontinuity at 500 nm is due to a change in optical filter during

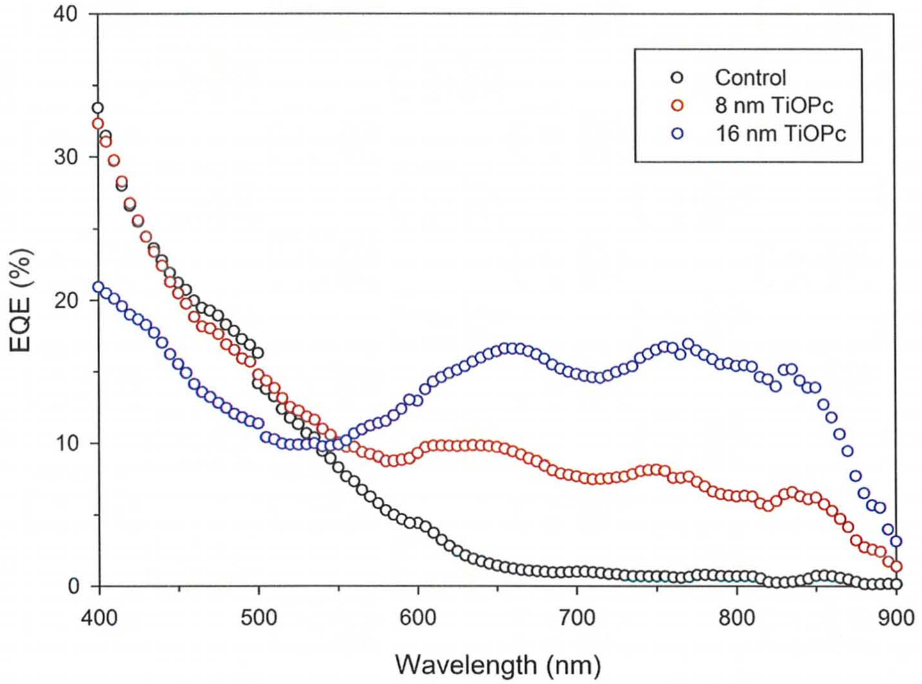

Figure 3.11: EQE curves for a range of thicknesses of TiOPc.

measurement. There is a marked increase in EQE values at long wavelengths and this can be attributed directly to the TiOPc. Some losses are apparent at lower wavelengths, especially in the 16 nm device, and as such it can be expected that there is a maximum point where gains from current generated at higher wavelengths are offset by losses at lower wavelengths.

The importance of the PEDOT:PSS interlayer is highlighted in Figure 3.12. J_{sc}, V_{oc} and FF are higher in cells containing PEDOT:PSS. Some of the improvement in FF can be attributed to reduced series resistance, likely brought on by better

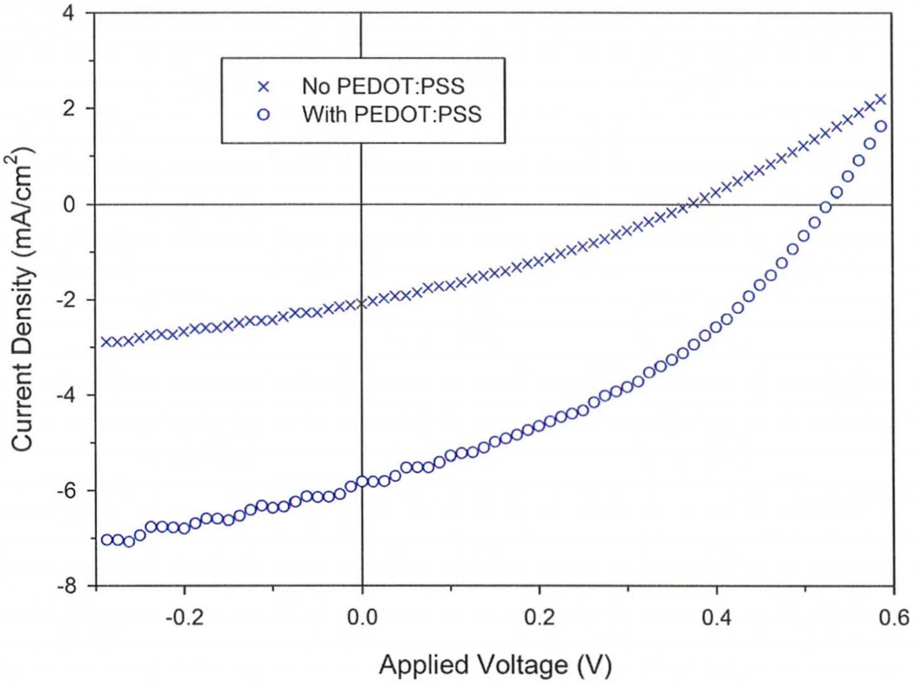

Figure 3.12: J-V curves for devices with and without a PEDOT:PSS buffer layer.

interlayer contact and improved charge collection. The resulting PCE is increased by a factor of four with the inclusion of the PEDOT:PSS interlayer. EQE curves shown in Figure 3.13 indicate that PEDOT:PSS improves current generation across the spectrum, which is important for ensuring proper integration of MPcs into OPV.

In summary, we have demonstrated V_{oc} and performance enhancement to the PQT-12/PCBM bulk heterojunction photovoltaic device with the introduction of MPc interlayers to the cell. V_{oc} increases in all cases over the control, often with a concomitant increase in J_{sc}. In the case of TiOPc the increased PCE is attributable

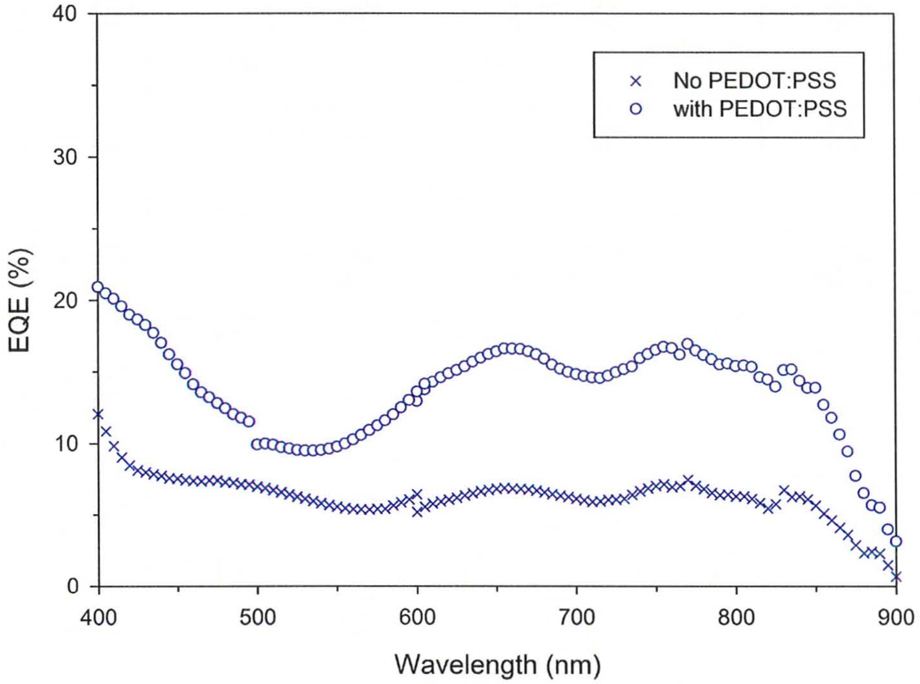

Figure 3.13: EQE curves for devices with and without a PEDOT:PSS buffer layer.

to increased absorption and current generation at wavelengths, up to 900 nm. The addition of the 16 nm TiOPc layer has shown significant device enhancement when included as an interlayer. PCE increases from 0.37% to 0.79% upon the addition of the TiOPc interlayer. Both the V_{oc} and J_{sc} increase while the FF remains intact. The TiOPc absorption profile and EQE indicate a polymorph transformation due to solvent contact during the spinning process. A partial conversion from amorphous to crystalline is likely also attributable to some gains in cell performance.

3.4 Heteromorphic ClInPc PV Devices

3.4.1 Preliminary Solvent Treatment Investigation for TiOPc and ClInPc

Up to this point, all polymorphic conversion has been performed by spinning solvent onto the surface of the MPc during deposition of upper layers of solution-processed material. This does not allow careful control of the solvent annealing process. Since exposure is via liquid contact during the spinning process, only specific solvents capable of dispersing the polymer and PCBM can be used. Also, each applicable solvent used in the spin coating process requires specific spinning parameters and solution temperature, making repeatability and side-by-side comparison between different solvents difficult. Direct liquid contact can also lead to MPc film damage and the formation of pinholes in the layer. Spinning directly with solvent also prevented an as-deposited film from being used as a baseline in any experiments. There was no feasible way to deposit the PQT-12/PCBM film without exposing the MPc layer to solvent. For these reasons a method of solvent annealing was needed that did not use solution processing.

Previous studies have investigated the use of vapour annealing as a means of repeatable film conversion [85–89, 93–95]. In the following study, solvent treatment was performed in a small chamber evacuated using a mechanical pump while liquid solvent was placed in a petri dish inside the chamber. The chamber was then allowed to reach equilibrium with the vapour pressure of the solvent at room temperature. Excess solvent was used so that some liquid phase always remained in the dish for the duration of the annealing process. The vacuum reduced the impact of water vapour and oxygen on cell characteristics and the chamber was also covered to reduce the amount of light entering. The remaining layers of the device were then vacuum deposited so as to prevent any additional polymorphic conversion from occurring.

Initial solvent tests were performed on TiOPc films as there was the most information describing solvent treatment and characterization of this MPc [85–92, 96]. Solvent treatment of TiOPc films with chloroform led to a distinct shift in the absorption spectra of the film, red-shifting the main peak from 720 nm to 830 nm, and broadening the entire absorption profile. This matched the literature well for Phase II [88, 92]. Figure 3.14 shows the UV-vis spectra of an untreated and treated film.

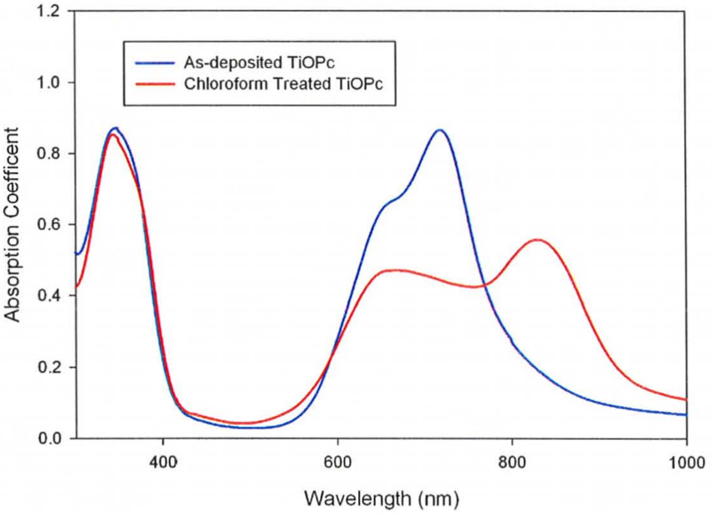

Figure 3.14: TiOPc thin film absorption spectra of as-deposited and chloroform treated films.

As can be seen, above 900 nm there is still measurable photon absorption in the film. Devices were fabricated using chloroform treated films on patterned ITO (~15 Ω/ □) coated aluminosilicate glass, 50 mm × 50 mm substrates. Films were deposited in a cryopump equipped thermal evaporator and a vacuum of 5 × 10^{-4} Pa was drawn before deposition. The device structure shown in Figure 3.15 consisted of 18 nm of TiOPc, followed by 30 nm of C_{60}, 10 nm of BCP and a 50 nm aluminum cathode. The initial TiOPc layer was either 1) untreated, as-deposited film, or 2) fully treated with chloroform for up to several hours. Solvent treatment was performed after initial TiOPc layer deposition. Slides were removed from vacuum and placed in the solvent treatment chamber for treatment. Following treatment, the slide was moved back into the vacuum chamber, and the remaining layers were then deposited.

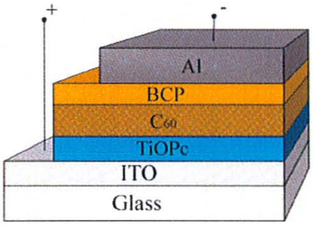

Figure 3.15: TiOPc/C_{60} vacuum deposited device structure.

J-V response curves shown in Figure 3.16 were measured using an Oriel solar simulator, illuminating the device through the ITO electrode with 100 mW/m^2 simulated sunlight. A Newport 818-UV/CM detector and Newport 1830-C optical power meter monitored input power. A Keithley 238 source-measure unit and PC collected

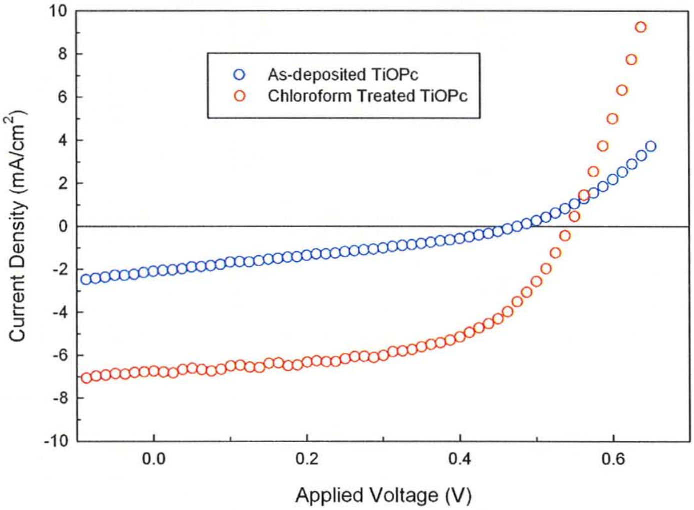

Figure 3.16: *J-V* response curves for as-deposited and chloroform annealed TiOPc/C_{60} PV devices.

output data. A shadow mask defined the active device areas as 7 mm^2.

Table 3.3: Device parameters for as-deposited and treated TiOPc device

Structure	**n(%)**	**V_{OC}**	**J_{sc}**	**FF**
18 nm TiOPc	0.31	0.48	2.09	31%
18 nm TiOPc Chloroform Treated	2.06	0.54	6.75	56%

Device characteristics of both the control and solvent treated samples are shown in Table 3.3. There is a clear improvement in efficiency brought upon by the solvent treatment of the TiOPc film. V_{oc}, J_{sc}, and FF are all higher in solvent treated devices, leading to a PCE of 2.06%, versus 0.31% in untreated devices of the same structure. The over three-fold improvement in J_{sc} is due to improved charge transport and current generation at higher wavelengths, seen in the EQE curves in Figure 3.17.

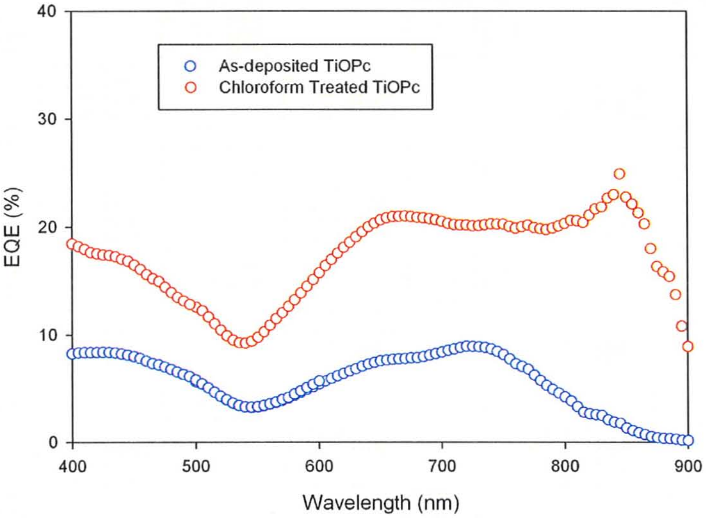

Figure 3.17: Effect of chloroform solvent treatment on the spectral response of TiOPc/C_{60} devices.

This trend matches the improvements seen in literature [87]. Solvent treatment with methanol and (1,2)dichlorobenzene was also tested using the same device structure however device characteristics were poor and showed no improvements in cell properties.

ClInPc is another MPc known to readily undergo polymorphic change when exposed to solvent [94, 97]. Films of this material have been shown to rearrange when exposed to CH_2Cl_2, and tetrahydrofuran (THF), broadening and redshifting the absorption spectra in a similar manner to TiOPc. This MPc is also attractive because it has one of the highest V_{oc} values of any MPc [98]. Solvent treatment of ClInPc films with a number of solvents, including chloroform, chlorobenzene and THF produced similar shifts in the absorption profile. The absorption band edge becomes strongly absorbing and extends beyond 850 nm. The as-deposited ClInPc peak and shoulder are at 724 nm and 658 nm respectively. There is also a weak absorption shoulder in the 800 to 820 nm range, indicating the presence of some infrared active polymorph [94]. Upon exposure to solvent, the 800 nm peak forms at the expense of the 724 nm peak [94]. The 658 nm shoulder remains strongly absorbing and becomes a peak at the expense of the 724 nm maximum. Figure 3.18 depicts the spectrum of

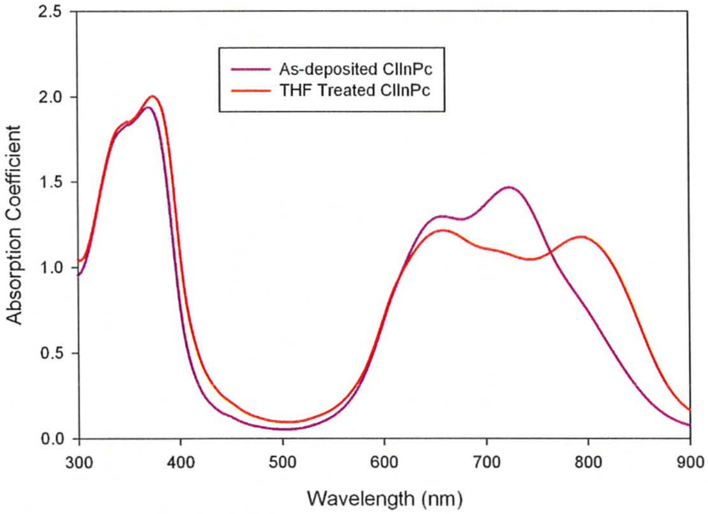

Figure 3.18: Optical absorption spectra of ClInPc thin film: (blue) as-deposited and (red) following exposure to THF.

ClInPc after exposure to THF for 20 minutes. Although many solvents tested produce the characteristic shift in the ClInPc absorption spectrum, fabrication of devices using the treated films were not necessarily as successful. Only one tested solvent, THF, reliably produced devices with enhanced photovoltaic characteristics. Some explanation should be given as to the reasoning behind the importance of solvent selection. Improper choice of solvent could potentially lead to excess film damage, causing pin-holes in the film and shorts in completed devices. The process of swelling and relaxation during polymorphic conversion of MPcs is not completely understood. The following section describes the investigation pertaining to the use of THF annealing for enhanced device characteristics.

3.4.2 Heteromorphic Study Using ClInPc

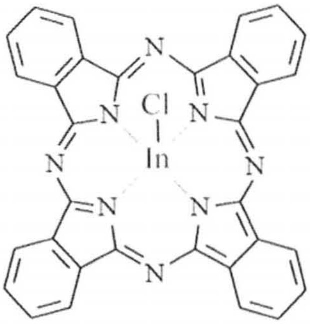

Figure 3.19: ClInPc molecular structure.

ClInPc, shown in Figure 3.19 is of particular interest in organic PV because it results in one of the highest open circuit voltages (V_{oc}) of any MPc in solar cells [98, 99]. Improving short circuit current (J_{sc}) without compromising V_{oc} in ClInPc based PV devices could offer an advantage over the more commonly studied CuPc in many solar cell applications. ClInPc shows clear broadening of Q-band absorption when exposed to solvent vapour [94]. THF has been shown to be a very effective solvent for phase transformation in trivalent MPcs and conversion can occur almost instantly [94]. In this study we investigated the impact of solvent annealing on the performance of ClInPc films used in PV and present a novel improved device structure integrating a heteromorphic bilayer of ClInPc.

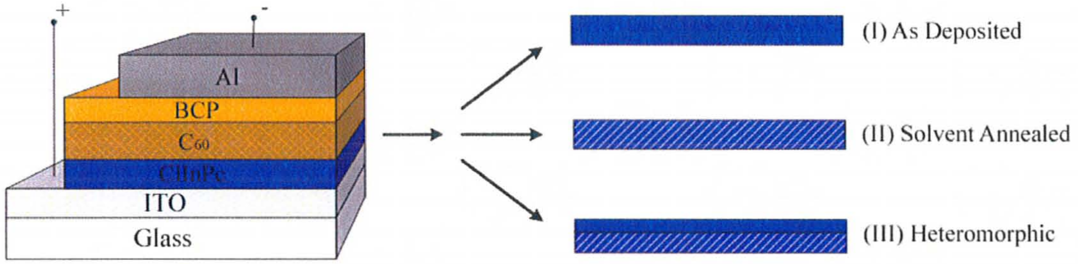

Figure 3.20: Three device structures of the evaporated ClInPc/C_{60} solar cell.

The device structure is shown in Figure 3.20. All devices contained a total of 16 nm of ClInPc. Structure (I) consists of solely as-deposited ClInPc and was not exposed to solvent, in Structure (II) the ClInPc layer is fully treated with solvent, and Structure (III) devices were prepared by exposing an initial 10 nm of ClInPc to solvent, followed by a 6 nm film of untreated ClInPc on top. The initial 10 nm layer was deposited so as to be thick enough to remain a continuous film after solvent treatment. In cases of thin MPc layers (~2 nm), films have been shown to aggregate into isolated crystallites on the surface of ITO [87].

Preliminary XRD analysis of as-deposited and THF treated ClInPc films was performed on coated glass substrates. Figure 3.21 shows X-ray diffraction spectra of the treated polymorph of ClInPc. The broad and weak amorphous spectra has been

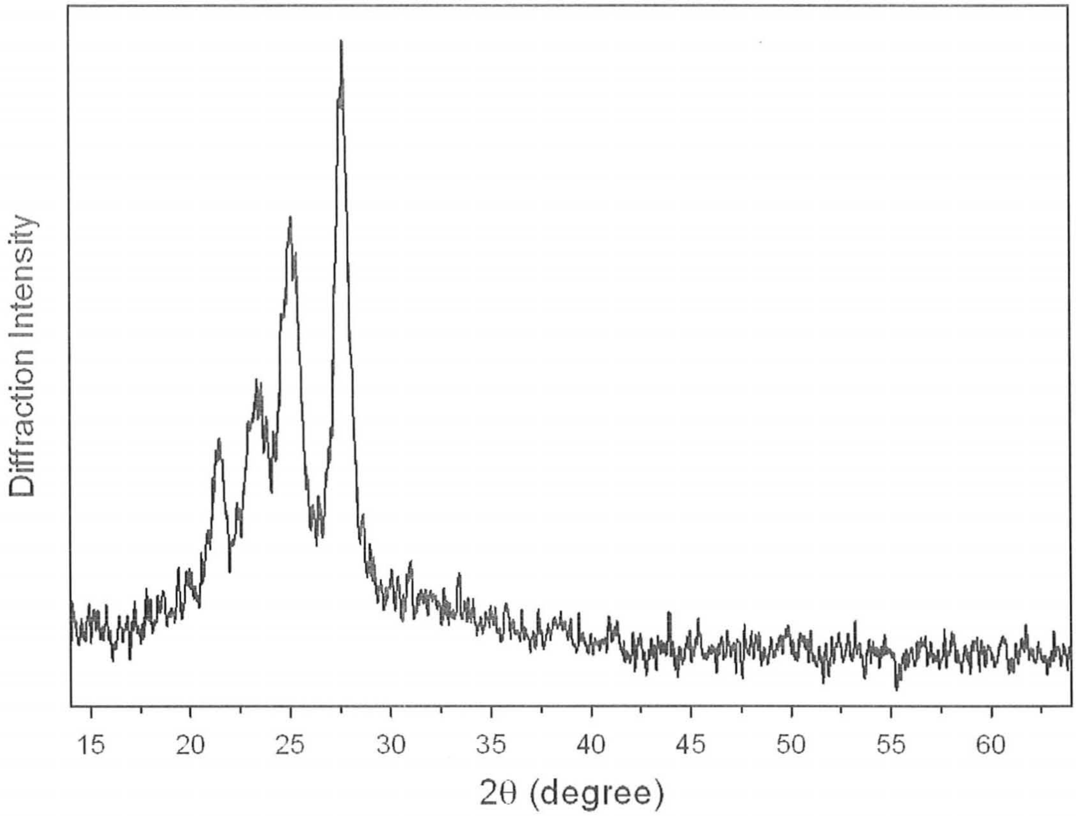

Figure 3.21: X-ray diffraction spectra of THF treated ClInPc thin films. The as-deposited spectra has been subtracted out.

subtracted from this plot. The THF treated ClInPc shows distinct diffraction peaks, indicating a degree of crystallinity in the film and the formation of a new phase. Peaks are located at 27.7 °, 25.1 °, 23.4 ° and 21.6 °, and match well with previous XRD analysis of the same phase [100, 101].

Photovoltaic devices were prepared on ITO (~15 Ω/ □) coated aluminosilicate glass, 50 mm × 50 mm substrates. The standard substrate cleaning procedure for vacuum deposited devices, as described in Section 3.2 was used. Substrates were transferred to a multiboat, multimask thermal evaporator for deposition. A vacuum of $< 4\times10^{-4}$ Pa was reached before material evaporation commenced. Structures (II) and (III) were removed from the vacuum chamber after initial ClInPc film deposition and transported to an isolated chamber where they were exposed to THF vapour for up to several hours. Structure (I) device performance was not affected by exposure of the bare ITO to THF solvent before initial layer deposition. Following initial ClInPc film preparation, the remaining device layers where deposited under vacuum. All three structures consisted of a 30 nm C_{60} layer, 10 nm BCP layer and a 50 nm aluminum cathode.

Devices were illuminated through the ITO electrode with 100 mW/cm^2 simulated sunlight using an Oriel 96000 solar simulator with an AM1.5G spectral filter. Input power was monitored with a Newport 818-UV/CM detector and Newport 1830-C optical power meter. A Keithley 238 source-measure unit and PC collected output data. The active device area was 7 mm^2 defined by a shadow mask. EQE measurements were performed using a calibrated monochromator from Photon Technology International and a Keithley 6485 picoammeter, measuring short circuit current as a function of incident wavelength.

The *J*-*V* characteristics for the three device structures are shown in Figure 3.22(a). Current densities were calculated by dividing the current by the active area. The efficiencies of Structure (I), (II) and (III) were 1.50%, 2.14% and 2.35% respectively. Both samples containing solvent treated ClInPc (Structure (II) and (III)) show a

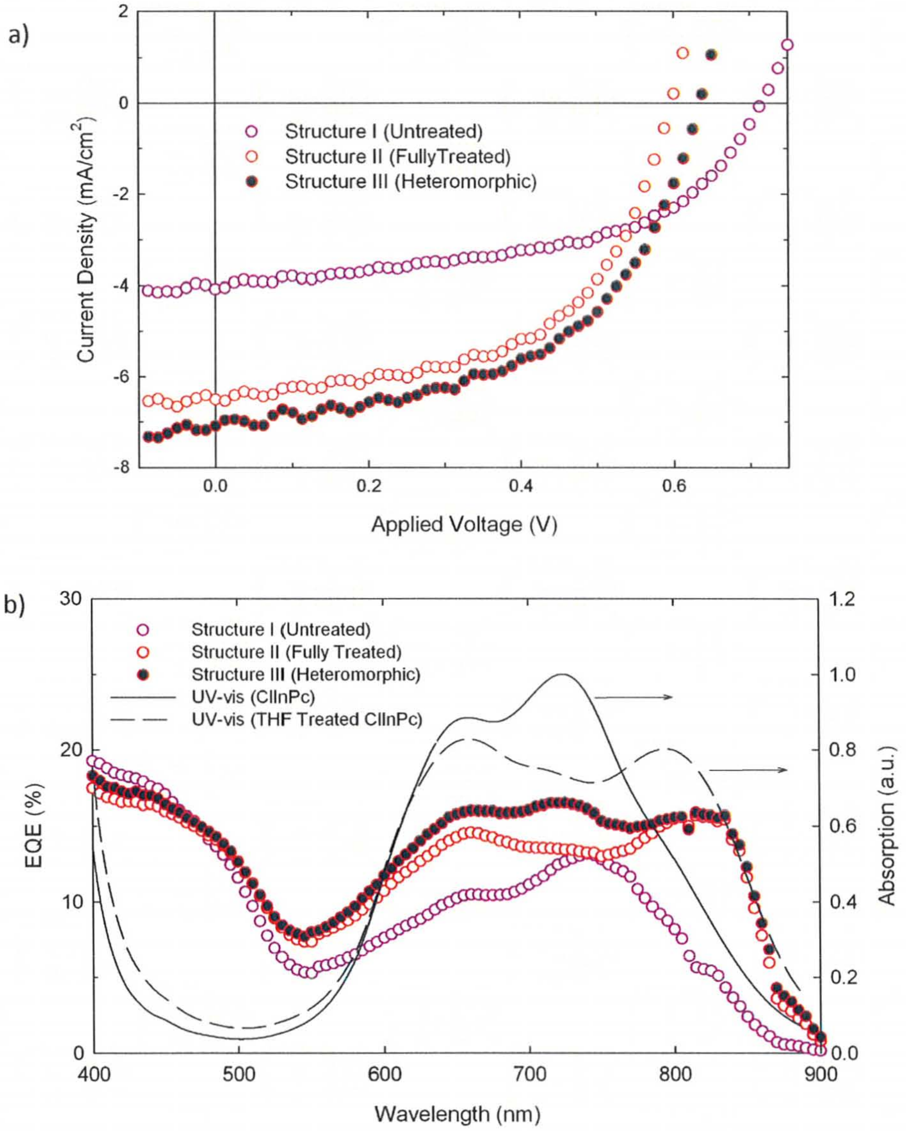

Figure 3.22: (a) *J*-*V* response curves showing the performance of devices incorporating ClInPc polymorphs. (b) EQE of ClInPc / C_{60} devices. UV-vis indicates the absorption profile of as-deposited ClInPc and THF treated films.

slightly reduced V$_{oc}$, however this drop is accompanied by a considerable increase in J$_{sc}$. Short circuit current increased from 4.08 mA/cm^2 in Structure (I) to 6.16 mA/cm^2 in Structure (II) to 7.09 mA/cm^2 in Structure (III). The heteromorphic device has the highest PCE and indicates an improvement in both V$_{oc}$ and J$_{sc}$ relative to Structure (II). The V$_{oc}$ of 0.63 V lies at an intermediary point between the V$_{oc}$ of Structure (I) and (II) (0.72 V and 0.59 V respectively). The increased J$_{sc}$ in other solvent treated devices has previously been attributed to improved cofacial contact area due to surface modification of MPcs films during exposure [87].

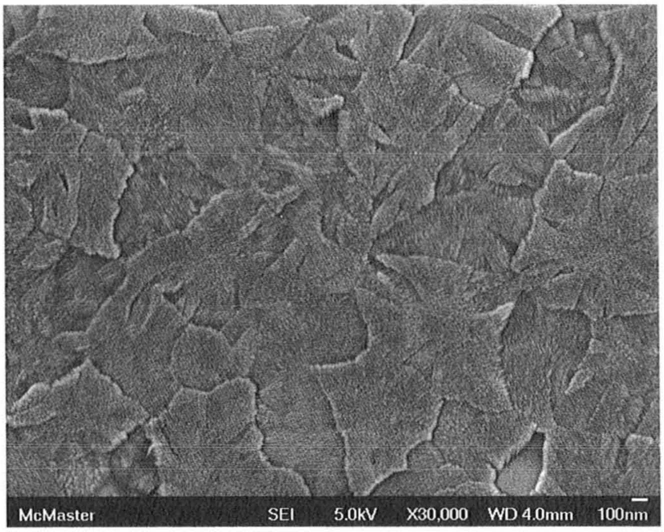

Figure 3.23: SEM image of bare ITO. Scale bar = 100 nm. Image taken by Gabriel Devenyi.

Since vacuum deposited MPc thin films conform to the underlying structure of the substrate, it can be assumed that the heteromorphic Structure (III) has similar surface features as the ITO electrode. With such a thin film, any substrate surface roughness can easily carry through the initially deposited ClInPc layers. The ITO

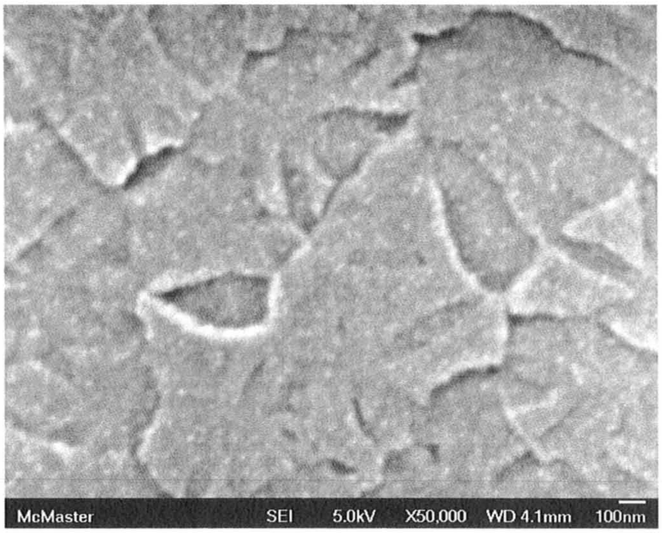

Figure 3.24: SEM image of a 10 nm film of untreated ClInPc. Scale bar = 100 nm. Image taken by Gabriel Devenyi.

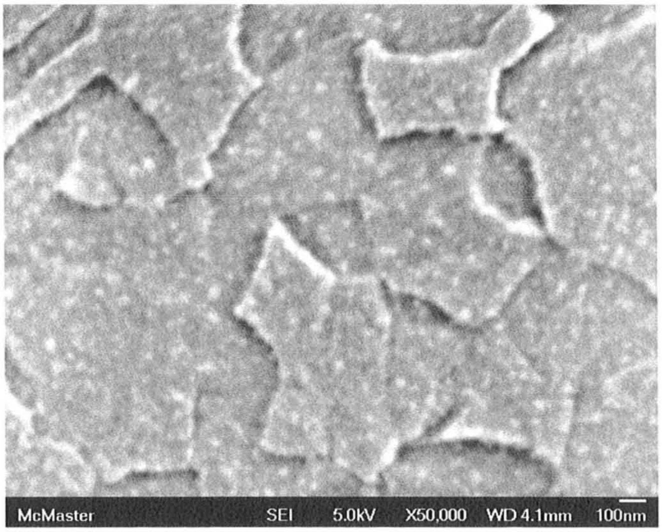

Figure 3.25: SEM image of a 10 nm film of treated ClInPc. Scale bar = 100 nm. Image taken by Gabriel Devenyi.

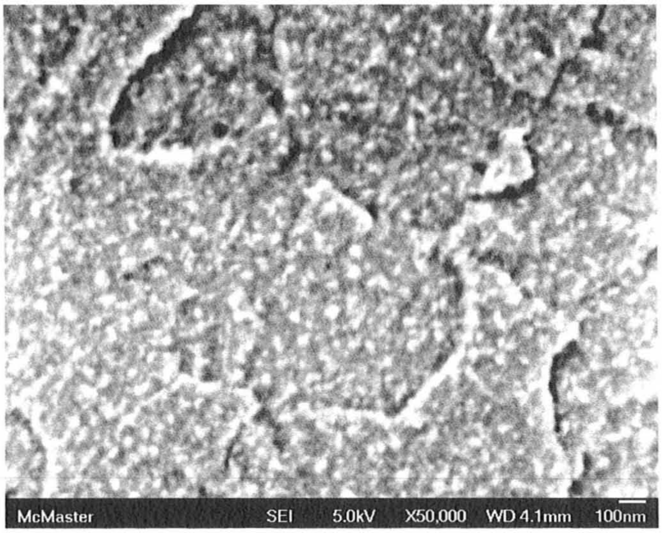

Figure 3.26: SEM image of a 16 nm heteromorphic structure of ClInPc. The film consists of a 10 nm of treated ClInPc with 6 nm of untreated ClInPc deposited on top. Scale bar = 100 nm. Image taken by Gabriel Devenyi.

surface shown in Figure 3.23 is generally not flat and under the SEM appears to be the main determinant of the surface features of the ClInPc film. Solvent treatment appears to only have a minimal effect on the surface roughness of films as seen by the differences between crystallite size in Figure 3.24 and Figure 3.25. The treated sample has slightly larger crystallites however the large ITO grain structures are completely dominant and appear to have a much larger feature size than any texturing due to the THF. Texturing can also be seen to carry through from the underlying 10 nm of treated ClInPc in the heteromorphic sample seen in Figure 3.26 however the ITO features are still obvious even with 16 nm of total film thickness. It is more likely that the main contributor to the increased efficiencies in solvent treated devices is in fact increased absorption and current generation at longer wavelengths. The higher photoactivity and improved transport properties gained by increases in crystallinity is also another likely contributor to improved device performance. The organized stacking decreases the average distance between ClInPc molecules and allows for stronger π-π interaction between molecules and therefore improved charge carrier mobilities.

The UV-vis absorption of evaporated and solvent treated ClInPc are shown in Figure 3.22(b). THF treated films show a distinct broadening to near-IR wavelengths after short exposure times. EQE results indicate improved current generation of the solvent treated samples within the Q-band absorption range of ClInPc in solvent treated samples. Structures (II) and (III) show extended absorption spectra and current generation beyond 850 nm. The EQE of Structure (III) also shows a heightened central peak at 725 nm, indicating a current contribution from the as-deposited ClInPc layer. This region is typically a valley as seen in the absorption profile of THF treated ClInPc.

Control of the polymorphic structures of MPcs have several advantages in PV devices. Firstly, integrating a bilayer of polymorphs of the same material reduces the number of raw materials necessary. Heteromorphic structures can also allow for optimal compromises between desirable properties of distinct polymorphs and lead to the fabrication of devices with a full spectrum of characteristics within the intermediary range of the properties of single phase.

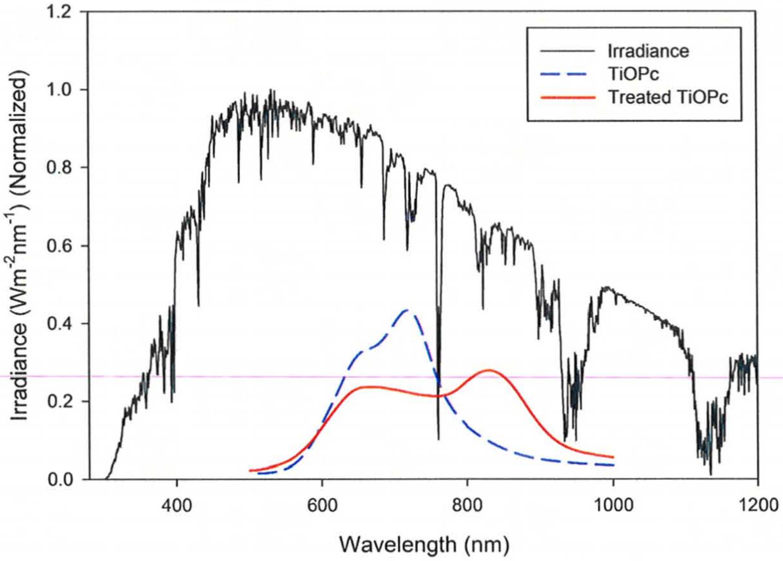

Figure 3.27: Absorption spectra of treated and untreated TiOPc compared to the solar spectrum.

Looking again at the solar spectrum, the importance of increased current generation at higher wavelengths can be seen in OPV. Improved current generation at longer wavelengths is important for improved matching of solar cell absorption to the solar spectrum. Lack of spectral overlap is a particular limitation in many organic PV materials, as described previously in Section 1.4.1. Polymorphic conversion is a useful method of shifting absorption to better match solar irradiance, as seen in Figure 3.27. Supplemental current at long wavelengths into the IR will result in a larger J_{sc} and therefore a greater maximum power point. Higher J_{sc} shifts the apex of the I-V downwards, leading to a maximum power point that is further from the origin, assuming the same V_{oc} and FF. A larger J_{sc} will then result in a higher PCE and therefore a greater energy output from the cell.

In summary, an improved ClInPc device structure has been fabricated and tested incorporating a heteromorphic bilayer. Polymorphic change has been induced in ClInPc films with solvent vapour exposure and the converted films show improved charge generation capability, as well as broadened absorption spectra, reaching beyond 850 nm. Increased J_{sc} could be attributable to improved interfacial contact between film and improved photoelectrical activity at longer wavelengths in the treated films. PCE has increased from 1.50% in the untreated structure to 2.35% in the heteromorphic device Structure (III). This dual phase bilayer has an intermediate V_{oc} allowing optimal *J-V* response, superior to that of either alternative structure. Phase control of other materials with a variety of polymorphic configurations could lead to improved performance in other devices.

3.5 Future Work

It is well known that other MPcs undergo phase changes. Investigating the PV behaviour of a variety of other MPcs that show solvent treatment conversions could yield impressive results if there is conversion to a highly photoactive phase. PV behaviour in polymorphs of VOPc, ClAlPc, ClAlClPc, ClGaPc, MgPc, ZnPc could be studied due to their ease of conversion [94, 100]. TiOPc is known to convert to several different polymorphs under suitable conditions and the possibility exists to study the various polymorphs of each MPc. Testing MPcs with a variety of other solvents could yield a superior phase or improved surface characteristics for use in organic photovoltaics.

Complete characterization of polymorphic phases of MPcs can be used for improved cell design and both material and phase choice in new device structures. Converted MPcs have been shown to be highly photoactive in some cases [93, 96]. Measuring time of flight (TOF) and fully characterizing molecular arrangement in these polymorphic forms could be advantageous.

Heteromorphic devices could in theory be fabricated with any MPc, or any materials that undergo controlled phase conversion. Investigating the effects of heteromorphic structures in other cell designs could lead to further efficiency improvements in other areas. Also, studies of the lifetimes of heteromorphic devices could determine if dual phase bilayers of the same material could be used for improved stability in organic photovoltaics.

3.6 Conclusions

Spectral coverage of OPVs can be improved by the introduction of MPcs into device architectures. The narrow spectral absorption of most conjugated polymers in the green-red region can be complemented by MPcs having strong light absorbing properties in the red and near-IR. MPc sensitivity can be further enhanced and red-shifted by polymorphic conversion, as has been verified with TiOPc and ClInPc. A more photoactive phase with improved properties has been integrated into PV devices for increased performance. Polymorphic conversion has been observed in a variety of MPcs, so a number of these materials have potential as near-IR and IR absorbers in PV. Controlled polymorphic conversion has been demonstrated in a variety of new cell configurations, showing improved charge generation capabilities and overall greater PCE.

Heteromorphic structures show promise for a variety of reasons. Any number of materials showing multiple metastable phases could be used in this type of configuration, and this is especially the case for the class of MPc molecules. Heteromorphic structures can reduce the likelihood of chemical interactions within the cell due to the need for fewer materials during fabrication. Interlayer reactions can be quite destructive in OPV, leading to shorter device lifetimes however using multiple phases of the same material could help counter this problem. Solvent treated and heteromorphic structures show improvement in light gathering capabilities and overall efficiency, indicating the distinct advantages of these structures and fabrication techniques. Solvent annealing has been shown to occur rapidly and controllably, and in addition there are a multitude of polymorphic states that can be investigated within the family of MPc materials.

Overall, light absorption and current generation have been improved using novel tandem and heteromorphic structures. Primarily, PCE has been enhanced in a number of cell configurations, indicating that these types of structures show promise as a means of improving efficiencies in OPV. Spectral mismatch has also been addressed in an effort to overcome one of the major limitations of OPV technology.

Bibliography

[1] T. Markvart and L. Castaner, *Practical Handbook of Photovoltaics: Fundamentals and Applications* (Elsevier Ltd., 2003).

[2] E. Lorenzo *et al.*, *Solar Electricity: Engineering of Photovoltaic Systems* (Earthscan Publications Ltd., 1994).

[3] C. W. Tang, Applied Physics Letters **48**, 183 (1986).

[4] G. Yu, J. Gao, J. C. Hummelen, F. Wudl, and A. J. Heeger, Science **270**, 1789 (1995).

[5] M. Reyes-Reyes, K. Kim, and D. L. Carroll, Applied Physics Letters **87**, 083506 (2005).

[6] H. Spanggaard and F. C. Krebs, Solar Energy Materials & Solar Cells **83**, 125 (2004).

[7] P. W. M. Blom, V. D. Mihailetchi, L. J. A. Koster, and D. E. Markov, Advanced Materials **19**, 1551 (2007).

[8] J. Xue, B. P. Rand, S. Uchida, and S. R. Forrest, Advanced Materials **17**, 66 (2005).

[9] G. Li *et al.*, Nature Materials **4**, 864 (2005).

[10] B. D. Boer and A. Facchetti, Polymer Reviews **48**, 423 (2008).

[11] G. Dennler and N. S. Sariciftci, Proceedings of the IEEE **93**, 1429 (2005).

[12] N. S. Sariciftci, Progress in Quantum Electronics **19**, 131 (1995).

[13] C. J. Brabec, N. S. Sariciftci, and J. C. Hummelen, Advanced Functional Materials **11**, 15 (2001).

[14] P. Vanlaeke *et al.*, Solar Energy Materials & Solar Cells **90**, 2150 (2006).

[15] A. P. Yuen *et al.*, Journal of Applied Physics **105**, 016105 (2009).

[16] P. Vemulamada, G. Hao, T. Kietzke, and A. Sellinger, Organic Electronics **9**, 661 (2008).

[17] B. S. Ong, Y. Wu, P. Liu, and S. Gardner, Advanced Materials **17**, 1141 (2005).

[18] B. S. Ong, Y. Wu, P. Liu, and S. Gardner, Journal Of The American Chemical Society **126**, 3378 (2004).

[19] E. Bundgaard and F. C. Krebs, Solar Energy Materials & Solar Cells **91**, 954 (2007).

[20] B. C. Thompson and J. M. Fréchet, Angewandte Chemie **47**, 58 (2008).

[21] K. Y. Law, Chemical Reviews **93**, 449 (1993).

[22] R. D. Gould, Coordination Chemistry Reviews **156**, 237 (1996).

[23] J. M. Robertson, Journal of the Chemical Society , 615 (1935).

[24] J. M. Robertson, Journal of the Chemical Society , 1195 (1936).

[25] J. M. Robertson and I. Woodward, Journal of the Chemical Society , 219 (1937).

[26] J. M. Robertson and I. Woodward, Journal of the Chemical Society , 36 (1940).

[27] D. R. Tackley, G. Dent, and W. E. Smith, Physical Chemistry Chemical Physics **3**, 1419 (2001).

[28] B. Joseph and C. S. Menon, E-Journal Of Chemistry **5**, 86 (2008).

[29] W. Herbst and K. Hunger, *Industrial organic pigments: production, properties, applications, 3rd edition* (Wiley-VCH, 2004).

[30] E. A. Lucia and F. D. Verderame, The Journal of Chemical Physics **48**, 2674 (1968).

[31] A. T. Davidson, The Journal of Chemical Physics **77**, 168 (1982).

[32] P. E. Fielding and F. Gutman, The Journal of Chemical Physics **26**, 411 (1957).

[33] H. J. Wagner, R. O. Loutfy, and C. Hsiao, Journal of Materials Science **17**, 2781 (1982).

[34] G. Ruani, C. Fontanini, M. Murgia, and C. Taliani, The Journal of Chemical Physics **116**, 1713 (2002).

[35] Y. Terao, H. Sasabe, and C. Adachi, Applied Physics Letters **90**, 103515 (2007).

[36] P. Peumans and S. R. Forrest, Applied Physics Letters **79**, 126 (2001).

[37] A. Ltaief, R. B. Chaâbane, A. Bouaziz, and J. Davenas, Materials Science and Engineering C **26**, 344 (2006).

[38] B. P. Rand, J. Genoe, P. Heremans, and J. Poortmans, Progress in Photovoltaics: Research and Applications **15**, 659 (2007).

[39] E. M. J. Johansson, A. Yartsev, H. Rensmo, and V. Sündstrom, Journal of Physical Chemistry C **113**, 3014 (2009).

[40] T. Taima, J. Sakai, T. Yamanari, and K. Saito, Solar Energy Materials & Solar Cells **93**, 742 (2009).

[41] F. Moser and A. Thomas, *Phthalocyanine Compounds* (Reinhold Publishing Corporation, 1963).

[42] H. Gommans *et al.*, Advanced Functional Materials **18**, 3686 (2008).

[43] J. Huang, J. Yu, H. Lin, and Y. Jiang, Journal of Applied Physics **105**, 073105 (2009).

[44] P. Peumans, V. Bulovic, and S. R. Forrest, Applied Physics Letters **76**, 2650 (2000).

[45] V. Tripathi, D. Datta, G. S. Samal, A. Awasthi, and S. Kumar, Journal of Non-crystalline Solids **354**, 2901 (2008).

[46] C. J. Brabec, S. E. Shaheen, C. Winder, and N. S. Sariciftci, Applied Physics Letters **80**, 1288 (2002).

[47] Y. Kim, A. M. Ballantyne, J. Nelson, and D. D. C. Bradley, Organic Electronics **10**, 205 (2009).

[48] V. Shrotriya, G. Li, Y. Yao, C. Chu, and Y. Yang, Applied Physics Letters **88**, 073508 (2006).

[49] F. S. Wen, W. L. Li, Z. Liu, and H. Z. Wei, Materials Chemistry and Physics **95**, 94 (2006).

[50] K. Sugiyama, H. Ishii, Y. Ouchi, and K. Seki, Journal of Applied Physics **87**, 295 (2000).

[51] M. Green, *Third Generation Photovoltaics* (Springer Series in Photonics, 2003).

[52] A. G. F. Janssen, T. Reidl, S. Hamwi, H.-H. Johannes, and W. Kowalsky, Applied Physics Letters **91**, 073519 (2007).

[53] J. Y. Kim *et al.*, Science **317**, 222 (2007).

[54] A. Colsmann, J. Junge, C. Kayser, and U. Lemmer, Applied Physics Letters **89**, 203506 (2006).

[55] G. Dennler *et al.*, Applied Physics Letters **89**, 073502 (2006).

[56] C. Zhang *et al.*, Applied Physics Letters **92**, 083310 (2008).

[57] A. P. Yuen *et al.*, A simple parallel tandem organic solar cell based on m-phthalocyanines, Manuscript in preparation.

[58] P. Peumans, A. Yakimov, and S. R. Forrest, Journal of Applied Physics **93**, 3693 (2003).

[59] R. F. Salzman *et al.*, Organic Electronics **6**, 242 (2005).

[60] I. Kaulach *et al.*, The European Physical Journal Applied Physics **40**, 169 (2007).

[61] B. Maennig *et al.*, Applied Physics A **79**, 1 (2004).

[62] J. Drechsel *et al.*, Thin Solid Films **451-452**, 515 (2004).

[63] J. Gao, G. Yu, and A. J. Heeger, Advanced Materials **10**, 692 (1998).

[64] D. Schlettwein and N. R. Armstrong, The Journal of Physical Chemistry **98**, 11771 (1994).

[65] R. O. Loutfy and Y. C. Cheng, The Journal of Chemical Physics **73**, 2902 (1980).

[66] H. Vestweber and W. Riess, Synthetic Metals **91**, 181 (1997).

[67] W. Gao and A. Kahn, Applied Physics Letters **79**, 4040 (2001).

[68] J. C. Bernède, H. Derouiche, and V. Djara, Solar Energy Materials & Solar Cells **87**, 261 (2005).

[69] A. J. Breeze, A. Salomon, D. S. Ginley, and B. A. Gregg, Applied Physics Letters **81**, 3085 (2005).

[70] S. Yu *et al.*, Dyes and Pigments **76**, 2008 (492-498).

[71] D. Tian *et al.*, Advanced Materials **21**, 37443749 (2009).

[72] X. Kong, M. Wang, S. Lei, Y. Yang, and C. Wang, Journal of Materials Chemistry **16**, 4265 (2006).

[73] S. Taira, T. Miki, and H. Yanagi, Applied Surface Science **143**, 23 (1999).

[74] T. D. Cano, J. A. de Saja, and R. F. Aroca, Chemical Physics Letters **377**, 347 (2003).

[75] J. K. J. van Duren, A. Dhanabalan, P. A. van Hal, and R. A. J. Janssen, Synthetic Metals **121**, 1587 (2001).

[76] D. Mühlbacher *et al.*, Advanced Materials **18**, 2884 (2006).

[77] L. Shen *et al.*, Applied Physics Letters **92**, 073307 (2008).

[78] B. P. Rand, J. Xue, F. Yang, and S. R. Forrest, Applied Physics Letters **87**, 233508 (2005).

[79] S. Jenekhe and S. Yi, Advanced Materials **12**, 1274 (2000).

[80] R. Koeepe, N. S. Sariciftci, P. A. Troshin, and R. N. Lyubovskaya, Applied Physics Letters **87**, 244102 (2005).

[81] C. J. Brabec *et al.*, Advanced Functional Materials **11**, 374 (2001).

[82] A. J. Moulé *et al.*, The Journal Of Physical Chemistry C **112**, 12583 (2008).

[83] C. A. Jennings, R. Aroca, G. J. Kovacs, and C. Hsaio, Journal of Raman Spectroscopy **27**, 867 (1996).

[84] H. Yonehara *et al.*, Chemistry of Materials **13**, 1015 (2001).

[85] J. Mizuguchi, G. Rihs, and H. R. Karfunkel, The Journal of Physical Chemistry **99**, 16217 (1995).

[86] T. D. C. no, V. Parra, M. L. Rodriguez, R. F. Aroca, and J. A. D. Saja, Applied Surface Science **246**, 327 (2005).

[87] D. Placencia *et al.*, Advanced Functional Materials **19**, 1913 (2009).

[88] H. S. Nalwa, T. Saito, A. Kakuta, and T. Iwayanagi, The Journal of Physical Chemistry **97**, 10515 (1993).

[89] T. Saito, W. Sisk, T. Kobayashi, S. Suzuki, and T. Iwayanagi, The Journal of Physical Chemistry **97**, 8026 (1993).

[90] T. Tsuzuki, Y. Kuwabara, N. Noma, Y. Shirota, and M. Willis, Japanese Journal Of Applied Physics **35**, L447 (1996).

[91] J. Conboy *et al.*, Journal of Physical Chemistry B **102**, 4516 (1998).

[92] M. Brumbach, D. Placencia, and N. R. Armstrong, The Journal of Physical Chemistry C **112**, 3142 (2008).

[93] A. M. Hor and R. O. Loutfy, Thin Solid Films **106**, 291 (1983).

[94] R. O. Loutfy, A. M. Hor, and A. Rucklidge, Journal of Imaging Science **31**, 31 (1987).

[95] T. Akazawa and Y. Takatsuka, Molecular Crystals and Liquid Crystals **471**, 213 (2007).

[96] W. Wang, X. Li, S. Wang, and W. Hou, Dyes and Pigments **72**, 38 (2007).

[97] R. O. Loutfy and A. M. Hor, Second Internet Conference on Photochemistry and Photobiology **2**, 759 (1983).

[98] A. P. Yuen *et al.*, Photovoltaic properties of m-phthalocyanine/fullerene organic solar cells, Under review by Journal of Applied Physics.

[99] A. M. Hor, R. O. Loutfy, and C. K. Hsiao, Applied Physics Letters **42**, 165 (1983).

[100] R. O. Loutfy, A. M. Hor, G. DiPaola-Baranyi, and C. K. Hsiao, Journal of Imaging Science **29**, 116 (1985).

[101] J. Ye, H. Chen, and M. Wang, Journal of Materials Science **38**, 4021 (2003).